POLITECNICO DI TORINO

Master's Degree
in Mathematical Engineering

Master's Degree Thesis

Computational study on the whistler instability

Supervisor
prof. Gianni Coppa

Candidate
Elena Fini

Assistant Supervisors
Dr. Gian Luca Delzanno
Los Alamos National Laboratory (NM, US)

Dr. Vadim Roytershteyn
Space Science Institute (CO, US)

Academic Year 2019-2020

Contents

English abstract

Whistler waves are electromagnetic waves that propagate in plasma; they can be observed in the Earth's magnetosphere, where they are responsible for the acceleration and precipitation of electrons.

Whistler waves are generated by the whistler instability, which is a plasma instability driven by the temperature anisotropy of warm electrons (energy ∼keV). Cold electrons (energy ∼eV) are usually present too and are thought to passively affect the developing whistler waves.

The present master thesis addresses the problem of studying with PIC methods the whistler instability in a plasma composed by both warm and cold electrons. The aim is to determine how the latter affects the maximum growth rate and the saturated amplitude of the waves generated by the instability.

Italian abstract

Le onde di whistler sono onde elettromagnetiche che si propagano nel plasma; le si può osservare nella magnetosfera terrestre, dove sono responsabili dell'accelerazione e della precipitazione degli elettroni.

Le onde di whistler sono generate dall'instabilità di whistler, un'instabilità del plasma alimentata dall'anisotropia nella temperatura degli elettroni caldi (con energia dell'ordine del keV). Solitamente è presente anche una popolazione di elettroni freddi (con energia dell'ordine dell'eV); gli elettroni freddi influenzano passivamente le caratteristiche delle onde di whistler così generate.

La presente tesi magistrale affronta il problema dello studio, con metodi PIC, dell'instabilità di whistler in un plasma composto sia da elettroni caldi che da elettroni freddi. L'obbiettivo è quello di determinare come questi ultimi influenzino il massimo tasso di crescita e il valore di saturazione dell'ampiezza delle onde di generate dall'instabilità.

Symbols

e	absolute value of the electric charge of the electron
k_B	Boltzmann constant
ε_0	vacuum permittivity
μ_0	vacuum permeability
c	speed of light in a vacuum
m_e	electron mass
m_i	ion mass
p	pressure
T	temperature
$\boldsymbol{E}$	electric field
$\boldsymbol{B}$	magnetic field
ρ	volumetric electric charge density
n_e	volumetric electron number density
n_i	volumetric ion number density
$\boldsymbol{j}$	current density
i	imaginary unit
λ	wavelength
$\boldsymbol{k}$	angular wavenumber
ω	angular frequency

Plasma parameters (in mks units)

General parameters

$\omega_{ce} = \frac{eB}{m_e}$	electron gyrofrequency
$\omega_{ci} = \frac{eB}{m_i}$	ion gyrofrequency
$\omega_{pe} = \sqrt{\frac{n_e e^2}{\varepsilon_0 m_e}}$	electron plasma frequency
$\omega_{pi} = \sqrt{\frac{n_i e^2}{\varepsilon_0 m_i}}$	ion plasma frequency
$\lambda_D = \sqrt{\frac{\varepsilon_0 k_B T_e}{n e^2}}$	Debye Length
$d_e = \frac{c}{\omega_{pe}}$	Plasma inertial length

Velocities

$\theta_{Te} = \sqrt{\frac{k_B T_e}{m_e}}$	electron thermal velocity
$\theta_{Ti} = \sqrt{\frac{k_B T_i}{m_i}}$	ion thermal velocity

Dimensionless parameters

$\alpha_e = \frac{\omega_{pe}}{\omega_{ce}}$	electron frequencies ratio
$\beta_e = 2\mu_0 \frac{n_e k_B T_e}{B_0^2}$	electron pressure to magnetic pressure ratio
$A = \frac{T_\perp}{T_\parallel}$	temperature anisotropy

Chapter 1

Introduction

The Earth's magnetosphere is formed by the interaction between the solar wind and the magnetic field of the Earth. It contains a plasma, i.e. an ionized gas made of electrons and ions. Several plasma particle populations exist in the magnetosphere. They can be broadly classified in terms of their energy: the cold and dense particles of the plasmasphere (energy ∼eV), the warm particles of the ring current and of the plasma sheet (energy ∼keV), and the rarefied, relativistic particles forming the Van Allen radiation belts (energy ∼MeV), to cite a few that are important for the work developed in this thesis.

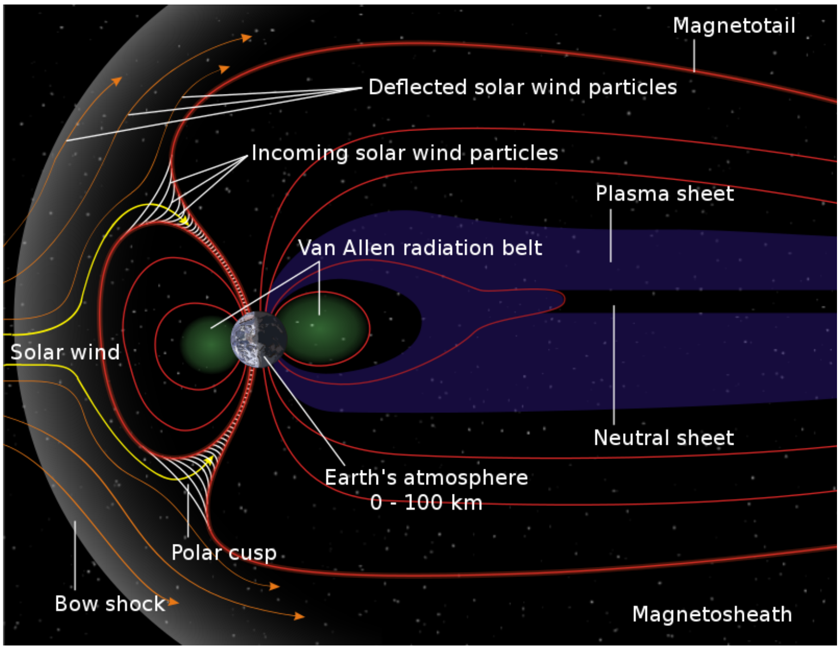

Figure 1.1: Diagram of Earth's magnetosphere. Image credit: NASA/Wikipedia (link).

The magnetospheric particle populations coexist with a variety of plasma waves. Waves are the "glue" of the magnetosphere: they couple the various particle populations by transferring energy between them. In this way, waves rule transport, energization and losses via the so-called wave-particle-interaction physics. Figure 1.2, taken from [1] (2010), shows a schematic representation of waves present in the inner magnetosphere which are particularly important from the point of view of phenomena controlling particle populations in the radiation belts.

These waves are whistler waves (called hiss and chorus), electromagnetic ion cyclotron (EMIC) waves and magnetosonic waves. Note that the inner magnetosphere is defined as the region of space from the Earth to near geostationary orbit (corresponding to an equatorial distance $r \sim 7\,R_E$, with R_E being the Earth radius equal to 6400 km).

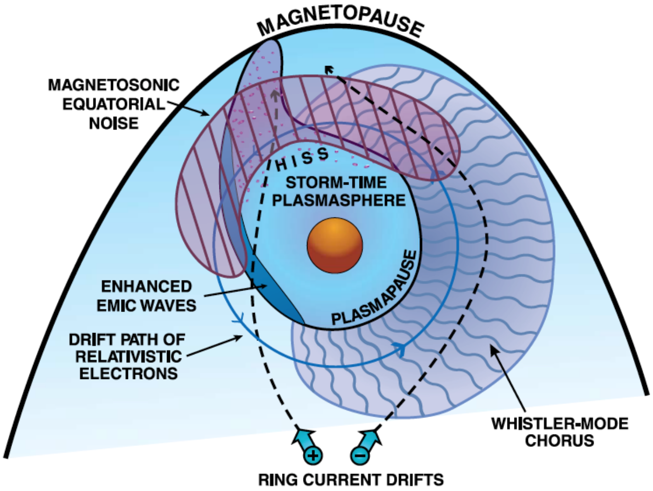

Figure 1.2: Representation of some of the waves that are important for inner magnetospheric physics and for the radiation belts in particular. From [1], (2010). Copyright AGU, reproduced with the permission from the publisher.

The focus of this thesis is on whistler waves, which are electromagnetic emissions with frequency below the electron cyclotron frequency. The name “whistler” originates from their first identification as radio waves from the ionosphere. These waves can can be generated by lightning and propagate along the field lines of the Earth’s magnetic field. Due to their characteristic dispersion relation, the lower frequencies whistler waves propagate slower than the higher ones. Consequently, these waves were detected by ground-based radio receivers as descending tones (“whistlers”) which can last for a few seconds. In the Earth’s magnetosphere, whistler waves have frequency in the kHz range. Whistler-mode chorus waves are discrete emissions often occurring in two distinct bands [2, 3, 4, 5], excited predominantly outside the plasmasphere (a near-Earth region of dense, cold plasma whose outer edge is called the plasmapause) [6]. Whistler waves They can interact resonantly with energetic electrons and are responsible for local acceleration [7, 8, 9] and scattering of such particles. The latter may as well as lead to losses of electrons via electron precipitation into the Earth's atmosphere in the form of diffuse [10] and pulsating aurora [11, 12] or microbursts [13, 14]. Whistler-mode hiss are incoherent, broadband emissions mostly found inside the plasmasphere [15, 16, 17, 18] and in plasmaspheric plumes [19]. They are mainly associated with losses of relativistic electrons [20].

It is well-known that whistler waves can be generated by an instability, called the whistler instability, driven by temperature anisotropy [21] in the electron energy distribution. This is believed to be the main generation mechanism for chorus waves. On the night side of the Earth's magnetosphere (i.e. the bottom part of figure 1.2), they are associated with the injection of warm ($\sim$keV) electrons from the plasma sheet during geomagnetic substorms. (Geomagnetic substorms are the periods of enhanced activity in the magnetosphere, characterized in particlur by perturbations in the magnetic field, release of energy from the "tail" of the magnetosphere, and enhanced activity (movement and brightening) of auroral arcs.

Figure 1.3: **Left:** Aurora australis (11 September 2005) as captured by NASA's IMAGE satellite, digitally overlaid onto The Blue Marble composite image. Image courtesy: NASA (link). **Right:** auorars appear as optical emissions ("Northern lights") in the atmosphere. Image credit: Jerry MagnuM Porsbjer/Wikipedia (link)

The whistler instability evolves to reduce the temperature anisotropy, driving the electron distribution towards marginally stable conditions where its growth rate is zero [22]. Recent works have used numerical simulations to parametrize the amplitude of the chorus waves created by the whistler instability in terms of initial plasma parameters and the strengths of the magnetic field [23, 24].

In this Master's thesis, we perform linear theory studies and non-linear simulations to investigate the impact of an additional population of cold electrons (with energy eV) on the whistler instability and on the generation of whistler waves. We note that this additional population is very often present in typical situations of interest in the Earth's magnetosphere. Additionally, it is well known that the cold electrons alter important properties of the whistler waves. For instance, the cold electrons lower the energy of the magnetospheric particles that interact resonantly with the waves and, since lower-energy particles typically have higher densities, this can lead to much stronger electron losses. Moreover, the cold electrons can alter the saturation amplitude of the whistler waves. This has very important implications for the Earth's magnetosphere, since the scattering and energization rates for resonant interaction between the magnetospheric particles and the waves depend on the wave amplitude. For instance, in the context of the so-called quasi-linear theory, the scattering/energization rates scale with the square of the wave amplitude. Hence changing the wave amplitudes strongly affects the dynamics of systems like the ring current, the plasma sheet and the radiation belts.

Despite the impact of cold electrons on the whistler instability in the Earth's magnetosphere has been known for a long time, to the best of our knowledge this is the first study that quantifies the saturation amplitude of the waves including cold electrons. In addition, we also include relativistic effects, showing that they can reduce the growth rate by $30 - 40\%$ relative to the standard treatment that does not include those effects. All together this work therefore delivers a very important physics-based result that can now be used in models of the near-Earth environment (such as ring-current models) where the waves are typically only treated empirically. For this reason, a manuscript based on the results of this Master's thesis is in preparation for submission to one of the leading space-physics journals.

Structure of the thesis

Chapters 2 and 3 will serve as a theoretical introduction to plasma, waves in plasma and one of the most notable approaches to mathematically model their propagation: the fluid dynamic modeling in cold plasmas. The cold plasma approximation will prove to be very useful in simplifying the theory of propagation; nonetheless, as will be exposed in chapter 4, the very nature of the whistler anisotropy instability requires the plasma to be treated as warm, with a more complicated description called kinetic theory.

Chapter 5 will sum up the results of the study on the whistler anisotropy instability. Those data were produced using two different approaches: firstly, by numerically solving the linearized, nonrelativistic equations describing waves in warm plasmas; secondly, by running computational simulations with a Particle-in-cell code that fully accounts for relativistic and nonlinear effects.

Chapter 2

Two-fluid modeling of cold and collisionless plasma

This chapter will serve as an introduction to plasmas and, more specifically, to one of its modeling techniques which is based on an analogy to fluid dynamics. The cold plasma approximation will be explained and then, in the following chapter, exploited along linear theory to deduce the dispersion relation of electromagnetic waves travelling through a plasma.

2.1 Preliminary notions

2.1.1 Plasma temperatures

Considering a classical Maxwellian distribution for the velocities in an ensemble of particles, the average kinetic energy is $E_{av} = \frac{1}{2}k_B T$ per degree of freedom. Due to this relationship between energy and temperature, it is common to describe a plasma using its kinetic temperature $k_B T$ and measuring it in electronvolts.

Collisionless plasma has the peculiarity to possess more than one temperature: each particle species usually has its own velocity distribution, and so its own temperature.

Furthermore, plasmas in space often have anisotropic temperature distributions for a single species, characterized by different temperature $T_\parallel$ and $T_\perp$ along and across the magnetic field.

2.1.2 Properties of the plasma: quasineutrality and collective behaviour

In the simplest case, a plasma originates from the ionization of a gas and is composed by two particle species: the negatively charged electrons and the positively charged ions,

But not every ionized gas shall be considered a plasma; a useful definition is the one given in [25, Section 1.2]: *"a plasma is a quasineutral gas of charged and neutral particles which exhibits collective behaviour"*.

Quasineutrality requires that, in a state of rest, the electrons and ions are present in similar quantities. Formally, one must have:

$$n_i \simeq n_e \equiv n \tag{2.1}$$

Where n_i and n_e are respectively the ions and electrons number densities.

Since particles in a plasma are subject - at least to some degree - to thermal motion, there might be occasional bunching of electrons or ions in a region of space. This creates an electrostatic potential, thus attracting particles of the opposite charge. This local potential affects the plasma only inside a sphere with the radius equal to the Debye length λ_D.

Recalling the definition of λ_D for the shielding of electric fields inside a plasma:

$$\lambda_D = \sqrt{\frac{\varepsilon_0 k_B T}{n e^2}} \tag{2.2}$$

Recalling then that outside of the Debye sphere quasineutrality is preserved, one could write the following, necessary but not sufficient, condition for the existence of a plasma (as we defined it):

$$\frac{\lambda_D}{L} \ll 1 \tag{2.3}$$

Where L is the characteristic length of the system. The plasma must remain, in its vast majority, quasineutral.

Turning our attention to the second property: collective behaviour means that particles are influenced not only by local conditions, but also by remote regions of the plasma. This is a consequence of the fact that plasmas respond to the electromagnetic force and the Coulomb interaction is long range.

This requires the motion of single particles not to be dominated by local forces and collisions. To avoid the first case, we must impose that the plasma is weakly coupled; which means the motion of a charged particle should not be dominated solely by the electrostatic field of another one in its proximity. Computations carried out in [26, Section 1.7] lead to the following formal condition:

$$N_D \gg 1 \tag{2.4}$$

Where N_D is the number of particles in a Debye sphere.

Lastly, we must require the time evolution of the plasma to not be dominated by collisions: the period τ_p of typical plasma oscillations shall be greater than the mean time τ between one random collision and another.

$$\frac{\tau}{\tau_p} > 1 \tag{2.5}$$

If the previous inequality is very strong, the plasma is said to be collisionless. Many astrophysical plasmas can be said to be collisionless, at least to a very good approximation.

2.1.3 The motion of charged particles

In plasma physics one generally works with the Maxwell equations in vacuum. We can recall these equations in their differential form:

$$\nabla \cdot \boldsymbol{E} = \frac{\rho}{\varepsilon_0} \tag{2.6}$$

$$\nabla \cdot \boldsymbol{B} = 0 \tag{2.7}$$

$$\nabla \times \boldsymbol{E} = -\frac{\partial \boldsymbol{B}}{\partial t} \tag{2.8}$$

$$\nabla \times \boldsymbol{B} = \mu_0 \boldsymbol{j} + \mu_0 \varepsilon_0 \frac{\partial \boldsymbol{E}}{\partial t} \tag{2.9}$$

Where ρ and $\boldsymbol{j}$ stands for the total charge and current density in the system.

A single charged particle moves under the influence of the Lorentz force, and in the absence of other forces its equation of motion is:

$$m\frac{d\boldsymbol{v}}{dt} = q\left(\boldsymbol{E} + \boldsymbol{v} \times \boldsymbol{B}\right) \tag{2.10}$$

Where m is its mass, v is its instantaneous velocity and q is its electric charge. The time derivative on the left side is to be taken at the position of the particle.

2.1.4 Why choosing a fluid dynamical approach

In a plasma we have a self-consistent problem to solve: we need to find particle trajectories that are determined by the equations of motion and that, following Maxwell equations, generate such electric and magnetic fields which eventually leads to the same equations of motion.

Fluid theory comes in handy since a typical plasma density might be 10^{18} ion-electron pairs per m^3,thus following the motion of single particles is computationally unfeasible.

Surprisingly, despite the many differences between plasma and fluids (mainly the fact that a fluid is driven into choerence by mechanical forces, while plasma is usually collisionless), plasma can be successfully modeled as two interpenetrating fluids: one for each species. This means that we no longer follow individual particles, but fluid elements of each species.

2.2 From Vlasov equation to the equations of motion

Following [26, Chapter 3] we will now introduce some basic concepts about the kinetic theory of plasmas. With the aid of appropriate approximations we will then derive a set of equations, analogous to the Navier-Stokes equations in fluid dynamics, to model the motion of a cold, collisionless plasma.

2.2.1 The Vlasov equation

We can define a phase-space density distribution function $F_s(\boldsymbol{r}, \boldsymbol{v}, t)$ for each particle species s. The distribution function can be used to obtain the number of particles which at time t are in a phase-space volume element $d^3\boldsymbol{r}\, d^3\boldsymbol{v}$ around $(\boldsymbol{r}, \boldsymbol{v})$.

If the plasma is collisionless, phase-space conservation requires that:

$$\frac{dF_s(\boldsymbol{r}, \boldsymbol{v}, t)}{dt} = 0. \tag{2.11}$$

Writing out the total time derivative on the left side, one obtains the Vlasov equation:

$$\frac{\partial F_s}{\partial t} + \boldsymbol{v} \cdot \nabla F_s + \boldsymbol{a_s} \cdot \nabla_v F_s = 0 \tag{2.12}$$

where $\boldsymbol{a_s}$ is the acceleration given by the Lorentz force on species s and ∇_v is the gradient operator in the velocity space.

Substituting the appropriate expression for the acceleration, equation 2.12 becomes:

$$\frac{\partial F_s}{\partial t} + \boldsymbol{v} \cdot \nabla F_s + \frac{q_s(\boldsymbol{E} + \boldsymbol{v} \times \boldsymbol{B})}{m_s} \cdot \nabla_v F_s = 0 \tag{2.13}$$

where q_s is the electric charge of species s and m_s is its mass.

The distribution function allows one to formulate the following two constitutive relations:

$$\rho = \sum_s q_s \int F_s(\boldsymbol{r}, \boldsymbol{v}, t) d^3\boldsymbol{v} \tag{2.14}$$

$$\boldsymbol{j} = \sum_s q_s \int \boldsymbol{v}\, F_s(\boldsymbol{r}, \boldsymbol{v}, t) d^3\boldsymbol{v} \tag{2.15}$$

for the charge density and the current density of the plasma. These equations, together with 2.6-2.9, are the Vlasov-Maxwell equation and represent a closed system that describes the time evolution of plasma.

Although the kinetic theory constitutes a reduction in complexity relative to treating the individual particle trajectories, the distribution function often provides way more information than what is necessary in practical applications. Also, being of high dimensionality (the distribution function is represented in a sixth-dimensional space composed of three spatial and three velocity coordinates plus time) and strongly non-linear, the Vlasov-Maxwell equations are very expensive to solve from a computational point of view.

A more efficient approach consists in building a set of fluid dynamics equations by deriving the statistical moments of 2.13, after recalling that the moment of order n of a function $f(\boldsymbol{r}, \boldsymbol{v}, t)$ is:

$$M_n = \int \boldsymbol{v}^n \, f \, d^3\boldsymbol{v} \tag{2.16}$$

2.2.2 The continuity equation

The zeroth order moment of 2.13 leads to the continuity equation for the conservation of a species mass (assuming no sources or losses):

$$\frac{\partial n_s}{\partial t} + \nabla \cdot (n_s \boldsymbol{u}_s) = 0 \tag{2.17}$$

where instead of particle velocity $\boldsymbol{v}$, we have the average velocity $\boldsymbol{u}_s$ of a fluid element of species s.

2.2.3 The momentum equation

After taking the first order moment of 2.13, neglecting viscosity and assuming isotropic pressure p - then carrying out several computations - one comes to the expression for the conservation of momentum:

$$n_s m_s \frac{D\boldsymbol{u}_s}{Dt} = -\nabla p + n_s q_s \left(\boldsymbol{E} + \boldsymbol{u}_s \times \boldsymbol{B}\right). \tag{2.18}$$

The derivative on the left hand is a material derivative, which serves as a link between the lagrangian and eulerian approaches. Indeed, for a generic vector property of the fluid element $\boldsymbol{A}(x,t)$ one has:

$$\frac{D\boldsymbol{A}}{Dt} = \frac{\partial \boldsymbol{A}}{\partial t} + (\boldsymbol{u} \cdot \nabla)\boldsymbol{A} \tag{2.19}$$

where $(\boldsymbol{u} \cdot \nabla)\boldsymbol{A}$ is the so-called convective term.

If the plasma is collisionless, as in this case, then all the particles inside a fluid element move together exactly with the average velocity.

Furthermore, if the plasma is cold, the pressure term on the right side can be neglected the since thermal velocity is much smaller than the flow velocity: the overall evolution of the system is not dominated by thermal motion.

The equation for the n-th moment requires the $(n+1)$-th moment and so one needs to make an assumption on the $(n+1)$-th moment in order to stop at some point - and this is called the closure of the equations. If the plasma is not cold, another equation is introduced to obtain closure: the energy equation, that is the second order moment of 2.13.

2.3 The closed set of equations

As previously mentioned, we will consider the simplest case of a plasma made of just two species: electrons (mass m_e and charge $-e$) and ions (mass m_i and charge e). This means we will have a two-fluid system, where each fluid will have its own continuity and momentum equation. Furthermore, the plasma is cold and so there is no need for an energy equation.

The plasma current density can be expressed as a function of number densities and fluid element velocities:

$$\boldsymbol{j} = e(n_i \boldsymbol{u}_i - n_e \boldsymbol{u}_e). \tag{2.20}$$

The number of scalar unknowns is therefore 14: two densities, six components of velocities, three component of the electric field and three components of the magnetic field.

In order to reach closure, the momentum and continuity equations have to be put together with the time-dependent pair of Maxwell's equations 2.8 and 2.9.

Ultimately, the complete set of equations for a cold and collisionless plasma is therefore:

$$m_e \frac{D\boldsymbol{u}_e}{Dt} = -e\left(\boldsymbol{E} + \boldsymbol{u}_e \times \boldsymbol{B}\right) \tag{2.21}$$

$$m_i \frac{D\boldsymbol{u}_i}{Dt} = e\left(\boldsymbol{E} + \boldsymbol{u}_i \times \boldsymbol{B}\right) \tag{2.22}$$

$$\frac{\partial n_e}{\partial t} + \nabla \cdot (n_e \boldsymbol{u}_e) = 0 \tag{2.23}$$

$$\frac{\partial n_i}{\partial t} + \nabla \cdot (n_i \boldsymbol{u}_i) = 0 \tag{2.24}$$

$$\nabla \times \boldsymbol{E} = -\frac{\partial \boldsymbol{B}}{\partial t} \tag{2.25}$$

$$\nabla \times \boldsymbol{B} = \mu_0 \boldsymbol{j} + \mu_0 \varepsilon_0 \frac{\partial \boldsymbol{E}}{\partial t} \tag{2.26}$$

Chapter 3

Cold electromagnetic waves in magnetized plasmas

Waves in plasmas can be differentiated in two groups: electrostatic and electromagnetic, depending on the existence of an oscillating magnetic field associated with the wave (electrostatic waves are those where the wave magnetic field is zero). This means that electrostatic waves are always longitudinal (the electric field oscillates along the direction of propagation $\boldsymbol{k}$ as can be easily seen from Faraday's law 2.9).

When a wave propagates with a velocity much higher than the species thermal velocity (which usually is the case for electromagnetic waves) then the cold plasma equations 2.21-2.26 can be used to describe the wave propagation. Indeed, "cold plasma wave" does not mean that the kinetic temperature of the plasma is low, but rather that the wave has a dispersion relation which does not depend on temperature [27, Chapter 6].

3.1 Waves in a magnetized plasma

We will consider a collisionless plasma permeated by a constant magnetic field directed along z-axis: $\boldsymbol{B}_0 = B_0\hat{\boldsymbol{z}}$.

Electromagnetic waves propagating in a magnetized plasma are usually classified according to the angle between their direction of propagation $\boldsymbol{k}$ and $\boldsymbol{B}_0$.

It should be recalled that Maxwell's equations allow only transverse waves in vacuum, which means that the electric and magnetic fields are always perpendicular not only to one another but also to the direction of propagation. However, electromagnetic waves in plasma are coupled to charge density waves coming from the motion of charged particles; this means that the resulting fields may have oscillating components along $\boldsymbol{k}$.

The presence of a background magnetic field introduces some additional parameters, which are the cyclotron frequencies of both electrons and ions. Assuming that electrons and ions have the same electric charge but with opposite sign, their cyclotron frequencies are expressed as following:

$$\omega_{ce} = \frac{eB_0}{m_e} \tag{3.1}$$

$$\omega_{ci} = \frac{eB_0}{m_i} \tag{3.2}$$

where e is the magnitude of the elementary charge, $e = 1.6\,10^{-19}$ C. This is the angular frequency associated with a circular motion, caused by Lorentz force, in the plane perpendicular to the magnetic field. This motion is called the gyromotion.

Other relevant parameters for the plasma system are the plasma frequencies, which are the angular frequencies associated with the electrons/ions oscillations due to a local displacement of charge, in a background situation of quasi-neutrality. They can be expressed as:

$$\omega_{pe} = \sqrt{\frac{n_e e^2}{\varepsilon_0 m_e}} \tag{3.3}$$

$$\omega_{pi} = \sqrt{\frac{n_i e^2}{\varepsilon_0 m_i}} \tag{3.4}$$

And their derivation comes from the study of plasma oscillations, as carried out in [25, Section 4.3].

3.2 From the equations of motion to the dispersion relation

The treating of the cold equations of motion 2.21-2.26 will roughly proceed through the following steps: the equations will be handled to obtain the so-called wave equation - a vector equation - which will be linearized; this will lead to a linear and homogeneous system of three scalar equations. In order to ensure a single, non-trivial solution, the determinant of the system will be computed and set equal to zero: this will finally produce the dispersion relation for the propagation of the electromagnetic waves in a plasma.

3.2.1 The wave equation

Let us consider the pair of time-dependent Maxwell equations 2.25 and 2.26. Applying the curl operator to both sides of 2.25 one has:

$$\nabla^2 \boldsymbol{E} - \nabla(\nabla \cdot \boldsymbol{E}) = \nabla \times \dot{\boldsymbol{B}} \tag{3.5}$$

while applying the time derivative to both sides of 2.26 leads to:

$$\nabla \times \dot{\boldsymbol{B}} = \mu_0 \frac{\partial \boldsymbol{j}}{\partial t} + \mu_0 \varepsilon_0 \ddot{\boldsymbol{E}} \tag{3.6}$$

(The dots denotes the first and second time derivative of a quantity. For further clarification on the notation used, refer to appendix A).

Finally, equating the left side of equation 3.5 and the right side of equation 3.6 leads to:

$$\mu_0 \frac{\partial \boldsymbol{j}}{\partial t} + \mu_0 \varepsilon_0 \ddot{\boldsymbol{E}} = -\nabla(\nabla \cdot \boldsymbol{E}) + \nabla^2 \boldsymbol{E} \tag{3.7}$$

From now on, we will refer to 3.7 as the wave equation.

3.2.2 Linearizing the equations

When working with time-varying quantities, such as in the case of electromagnetic waves in a plasma, it is useful to assume that oscillations have a small amplitude compared to the equilibrium values. Therefore the equations of motion can be linearized with the following procedure.

It is important to distinguish between equilibrium quantities, indicated with a 0 subscript, and perturbation quantities, indicated with a 1 subscript. Once equations 2.21-2.24 and 3.7 have been expanded in powers of perturbation quantities, only terms of order ≤ 1 will be retained, thus achieving linearization.

We will start with the following equilibrium conditions:

$$\begin{aligned}\boldsymbol{E}_0 &= 0\\ \boldsymbol{B}_0 &= B_0\hat{\boldsymbol{z}}\\ n_e &= n_i = n_0\\ \boldsymbol{v}_{e0} &= \boldsymbol{v}_{i0} = \boldsymbol{0}\end{aligned} \tag{3.8}$$

And we will assume that the wave frequency is sufficiently high, so that ions can be considered as a static and neutralizing background and only the electron motion contributes to the perturbed current density in the linearization of 2.20:

$$\boldsymbol{j} = \boldsymbol{j}_0 - n_0 e \boldsymbol{v}_{e1} \tag{3.9}$$

where, following the initial conditions stated above, $\boldsymbol{j}_0 = 0$. Then the linearized wave equation takes the form:

$$-\mu_0 n_0 e \frac{\partial \boldsymbol{v}_{e1}}{\partial t} + \mu_0 \varepsilon_0 \ddot{\boldsymbol{E}}_1 = -\nabla(\nabla \cdot \boldsymbol{E}_1) + \nabla^2 \boldsymbol{E}_1 \tag{3.10}$$

The linearized momentum equations are:

$$m_e \frac{\partial \boldsymbol{v}_{e1}}{\partial t} = -e(\boldsymbol{E}_1 + \boldsymbol{v}_{e1} \times \boldsymbol{B}_0) \tag{3.11}$$

Lastly, the linearized continuity equations are:

$$\frac{\partial n_{1e}}{\partial t} + \nabla \cdot (n_0 \boldsymbol{v}_{1e}) = 0 \tag{3.12}$$

$$\frac{\partial n_{1i}}{\partial t} + \nabla \cdot (n_0 \boldsymbol{v}_{1i}) = 0 \tag{3.13}$$

3.2.3 Solving the equations

The linearized equations 3.10-3.11 form a system of linear differential equations. The general solution for this kind of system can be expressed as a superposition of plane waves. For this reason we will use the following ansatz for perturbed quantities:

$$\begin{aligned}\boldsymbol{E}_1 &= \overline{\boldsymbol{E}}_1 e^{i(\boldsymbol{k}\cdot\boldsymbol{r}-\omega t)}\\ \boldsymbol{v}_{e1} &= \overline{\boldsymbol{v}}_{e1} e^{i(\boldsymbol{k}\cdot\boldsymbol{r}-\omega t)}\\ n_{e1} &= \overline{n}_{e1} e^{i(\boldsymbol{k}\cdot\boldsymbol{r}-\omega t)}\end{aligned} \tag{3.14}$$

Once this ansatz is made, the continuity and momentum equations will be used to find $\overline{n}_{e1}$ and $\overline{\boldsymbol{v}}_{e1}$ whose expressions will be inserted in the wave equation.

The wave equation will finally become a linear system of equations in the unknowns $\overline{E}_x$, $\overline{E}_y$ and $\overline{E}_z$. In order to ensure the existence of at least one non-trivial solution, the determinant of the associated matrix A must be equal to zero.

$$\det(A) = \mathrm{f}(\boldsymbol{k},\, \omega) = 0 \tag{3.15}$$

Equation 3.15 gives the **dispersion relation** of the wave.

3.2.4 Complex solutions of the dispersion relation and the growth rate

Assuming $\boldsymbol{k}$ to be real, the solution of equation 3.15 $\omega(\boldsymbol{k})$ is always real in the case of cold plasma; however, in other situations it may be complex. This means that it can be expressed as:

$$\omega = \omega_R + i\gamma \tag{3.16}$$

Where γ, the complex part, is called the *growth rate* of the wave.

It is straightforward to see that, if the growth rate is positive, the amplitude of the electric and magnetic field associated to the wave grows. For example, recalling expressions 3.14, one has:

$$\boldsymbol{E}_1 = \overline{\boldsymbol{E}}_1\, e^{i\boldsymbol{k}\cdot\boldsymbol{r}}\, e^{-i\omega_R t}\, e^{\gamma t} \tag{3.17}$$

The last term increases exponentially over time, leading - theoretically, at least - to the divergence of the electric field. In reality, the divergence of the amplitude is due to the linear theory assumption. In reality non-linear effects will lead to the saturation of the wave amplitude.

3.3 Whistler waves

Whistler waves is the name given to a specific plasma mode: these waves mainly propagate in a direction parallel to the imposed magnetic field, are right-hand polarized and with frequencies lower than ω_{ce} but higher enough to neglect ion motion.

This means that, if $\boldsymbol{B}_0$ lies along $\hat{\boldsymbol{z}}$, one shall make the following assumptions:

$$\boldsymbol{k} = k_z\hat{\boldsymbol{z}} \qquad \boldsymbol{E} = E_x\hat{\boldsymbol{x}} + E_y\hat{\boldsymbol{y}} \tag{3.18}$$

Applying the linear theory described before (while assuming the cold plasma approximation to still be valid) the resulting general dispersion relation is:

$$\frac{\omega_{pe}^2}{1 \mp \omega_{ce}/\omega} - \omega^2 + c^2k^2 = 0 \tag{3.19}$$

Which leads to two specific dispersion relations: one has left-hand polarization, while the other has right-hand polarization.

Considering the right-hand polarization:

$$\frac{\omega_{pe}^2}{1 - \omega_{ce}/\omega} - \omega^2 + c^2k^2 = 0 \tag{3.20}$$

One shall come to a dispersion relation plot qualitatively similar to the one in figure 3.1; we call *whistler waves* the waves which are found in red highlighted area. More details about the generation of whistler waves in warm plasmas will be added in the next chapter.

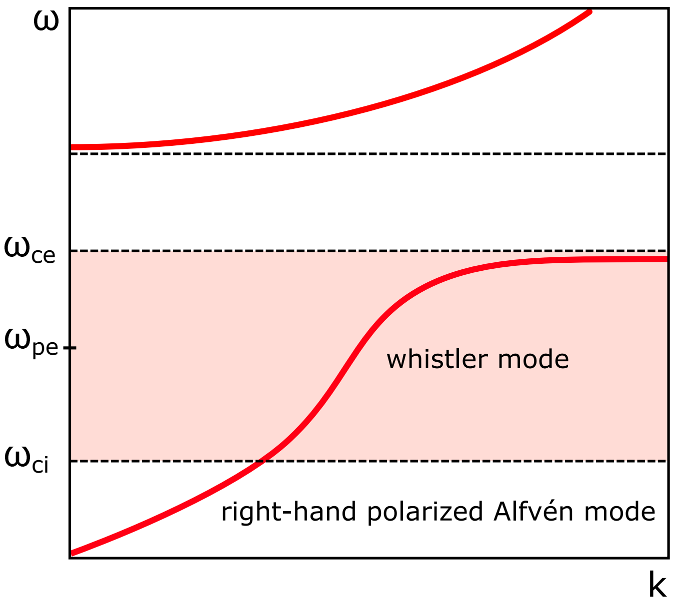

Figure 3.1: Whistler dispersion relation.

Chapter 4

The whistler anisotropy instability

Whistler waves have been studied for over 100 years [28]. The first evidence of their presence in the ionosphere came more than a century ago, when very low frequency radio waves were detected and translated into whistle-like sounds (hence the name whistler wave). Such whistles sound are descending tones lasting for a few seconds and were later found to be generated by lightnings.

Years later, many other phenomena in the Earth's ionosphere and magnetosphere were linked to chorus waves propagating in the whistler branch [29]: their name comes, again, from the sound obtained when translating the electromagnetic signals, which resembles the chirping of birds. Whistler chorus waves are electromagnetic emissions that usually occur in two distinct bands. They have been demonstrated to play a key role in electron scattering and precipitation [22] as well as in the dynamics of the plasma sheet and the radiation belt.

Whistler chorus waves are found to be mainly generated in space by the *whistler anisotropy instability*. In plasmas a wide range of instabilities can be triggered by different equilibrium conditions; this particular instability is caused by an initial electron temperature anisotropy and gives rise to unstable waves in the whistler mode.

4.1 Physical conditions triggering the instability

4.1.1 Anisotropic velocity distribution

We already hinted at the possibility to have different temperatures in a plasma and even in a single particle species.

We will assume the ion population is described by an isotropic maxwellian distribution; this makes the ions nonresonant with this instability [21], as ions do not respond to the fast electron scales and to zero-th order they can be assumed as a stationary background. The electron population, on the other hand, will display two different temperatures - depending on which velocity component, parallel or perpendicular, is considered: $T_\parallel$ and $T_\perp$.

Below is the reference expression for a bimaxwellian distribution function:

$$F(v_\perp, v_\parallel) = \frac{1}{(2\pi)^{3/2}} \frac{1}{\theta_\perp^2 \theta_\parallel} \exp\left[-\frac{1}{2}\left(\frac{v_\perp^2}{\theta_\perp^2} + \frac{v_\parallel^2}{\theta_\parallel^2}\right)\right] \tag{4.1}$$

$$\begin{aligned} \theta_\perp &= \sqrt{\frac{k_B T_\perp}{m_e}} \\ \theta_\parallel &= \sqrt{\frac{k_B T_\parallel}{m_e}} \end{aligned} \tag{4.2}$$

$\theta_\perp$ and $\theta_\parallel$ are the thermal velocities along directions parallel and perpendicular to $\boldsymbol{B}_0$.

Obviously, the presence of the temperature anisotropy violates the cold plasma assumption that we introduced in chapter 3. In this thesis, however, we are interested in studying the effect of a cold electron population on the temperature anisotropy instability that is driven by warm electrons. As we discussed in the introduction, this is a common situation for the Earth's magnetosphere where anisotropic plasmasheet electrons with keV energies are injected in the inner magnetosphere during geomagnetic substorms. They are energetically unstable and generate whistler chorus waves, but they often coexist with a population of colder electrons (energies ∼eV) which is important in determining the properties of the chorus waves.

4.1.2 Temperature anisotropy threshold

The degree of temperature anisotropy will be stated by the adimensional quantity $A = T_\perp/T_\parallel$. In order to excite the instability, the perpendicular temperature must be greater than the parallel one: $A > 1$.

4.2 Effect of cold electrons on whistler waves generated by the instability

The cold electrons have an isotropic distribution and are generally believed to have a passive effect on the whistler instability (which is driven by the anisotropy of the warm population) by modifying the total density and related parameters of the background plasma.

The presence of a cold electron population may be from now on quantified by the ratio n_c/n_e, where n_c is the cold electron number density and n_e is the total electron number density.

For instance, one can see by recalling the definition of electron plasma frequency:

$$\omega_{pe} = \sqrt{\frac{4\pi\, n_e\, e^2}{m_e}} \tag{4.3}$$

and the definition of electron inertial length:

$$d_e = \frac{c}{\omega_{pe}} \tag{4.4}$$

that, if the warm electrons density stays fixed, an injection of cold electrons causes the total electron density to increase: this leads to a larger electron plasma frequency and a smaller electron inertial length. Generally speaking the presence of cold electrons affects the characteristics of whistler waves generated by the whistler instability, even if the warm electrons have the main role in generating them.

In [30], via a numerical solver with no approximations nor relativistic corrections, linear theory was used to study the effect given by adding cold electrons to the warm, anisotropic population. The results showed that the maximum growth rate increases with increasing n_c/n_e but only up to some value ($n_c/n_e \sim 0.8$), where γ_{max} has a peak; it then starts to decrease very rapidly.

4.3 Parallel and oblique wave propagation

Let's firstly recall the definition of β, the ratio between plasma pressure and magnetic pressure:

$$\beta = 2\mu_0 \frac{n\, k_B\, T}{B_0^2} \tag{4.5}$$

A very relevant parameter in the following study will be $\beta_\parallel$:

$$\beta_\parallel = 2\mu_0 \frac{n_h\, k_B\, T_\parallel}{B_0^2} \tag{4.6}$$

Which is β computed with the parallel temperature of the warm anisotropic electrons.

It has been verified (see [31] and [23]) by theory and PIC simulations that, for low enough values of $\beta_\parallel$ (~ 0.025), the waves excited by the whistler instability switch their propagation direction from parallel - with respect to the external magnetic field - to oblique.

Since the following work is meant to focus only on the study of parallel propagation, it will be crucial to ensure that the value of $\beta_\parallel$ always stays above this critical value (which will be denoted as $\beta_\parallel^*$).

In [30] it was found that the presence of cold electrons affect the critical value with the following scaling law:

$$\beta_\parallel^* = 0.0245\,[1 - 1.05(n_c/n_e)] \tag{4.7}$$

Chapter 5

Computational study of the whistler instability

As discussed in the previous chapter, the whistler instability is triggered in warm plasmas by an anisotropic temperature distribution: this means that temperature effects cannot be disregarded. Cold plasma theory and the fluid dynamics approach cannot be used to study the instability, whose correct description requires the solution of the full Vlasov equation simultaneously with Maxwell's equations. In this work Particle-in-cell (PIC) 1D simulations have been used to study the onset and the evolution of the whistler instability in various conditions that should be relevant to the environment of the Earth's magnetosphere.

VPIC[32] [33] [34] was the code of choice: it is a three-dimensional Particle-in-cell code for modeling kinetic plasma with a second-order, explicit algorithm to update positions and velocities of charged particles in order to solve the relativistic kinetic equation for each species in the plasma. Electric and magnetic fields are made to evolve accordingly via a second-order finite-difference-time-domain method.

First the details of the physical setup of the simulations will be explained, along with an overview of parameters and constants. Then the results from different series of simulations, where these parameters vary, will be presented.

The quantities of interest for the study are the instability maximum growth rate γ and the saturation value of the magnetic perturbation $\delta B/|\boldsymbol{B}_0|$ (see eq. 5.1): those quantities have been extrapolated from the data produced by VPIC as shown in figure 5.1. Indeed, figure 5.1 represents an example of data obtained from a typical run: there is a linear phase clearly identifiable, from which one can estimate the growth rate; after that a saturation phase occurs. The saturation value is critical because it is the amplitude of the waves that controls processes such as scattering and energization, which rule the dynamics of the ring current and radiation belts.

VPIC results will be compared with those from a linear solver of the Vlasov and Maxwell's non-relativistic equations (based on chapter 11 of [35]). Data from already existing studies will be also used for comparison, so that the reliability of the software is corroborated.

Post-processing analysis was carried out with the aid of MATLAB and Python scripts.

The expression used to compute the magnetic perturbation was the following:

$$\frac{\delta B}{|\boldsymbol{B}_0|} = \frac{1}{|\boldsymbol{B}_0|}\sqrt{\frac{1}{n_z}\sum_{j=1}^{n_z}\left(B_x^2 + B_y^2\right)} \tag{5.1}$$

where n_z is the number of cells in the $\hat{z}$ direction. Note that in equation 5.1 we have used only the components of the wave field perpendicular to the background magnetic field. This is because for the field-aligned waves considered here the component of the wave field along z is zero.

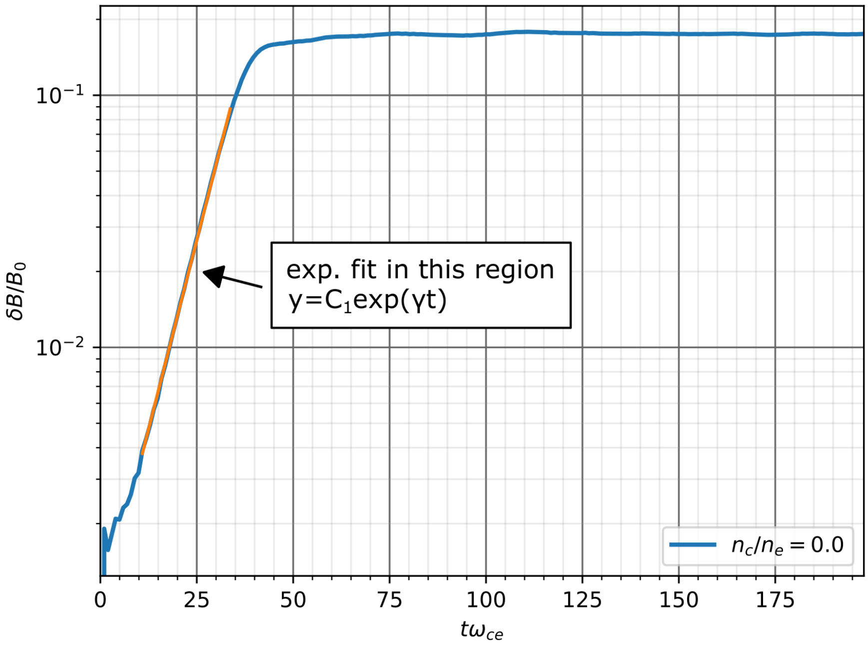

Figure 5.1: Example, with log-y scale, of how the magnetic perturbation exponential growth was fitted with a Python script. This specifical example was obtained with the parameters: $A = 5$, $\beta_{\|} = 0.15$ and $n_c/n_e = 0$.

5.1 Linear nonrelativistic theory applied to warm plasmas

The following section outlines, through linear kinetic theory, the propagation of electromagnetic waves in a warm plasma subjected to an external magnetic field $\boldsymbol{B}_0$ (for a more detailed analysis see [26], Chapter 6). The final result will be a set of linearized, nonrelativistic equations that can be solved numerically.

Let us consider a plasma composed just of electrons, with charge $-e$ and mass m_e, and ions with charge e and mass m_i. The linearization procedure exposed in 3.2.2 could be applied to the Vlasov equation: assuming an equilibrium distribution function F_{s0} and a small-amplitude perturbation F_{s1}, equation 2.13 becomes:

$$\frac{\partial F_{s1}}{\partial t} + \boldsymbol{v} \cdot \nabla F_{s1} + \frac{q_s}{m_s}(\boldsymbol{v} \times \boldsymbol{B}_0) \cdot \nabla_v F_{s1} = -\frac{q_s}{m_s}(\boldsymbol{E} + \boldsymbol{v} \times \boldsymbol{B}) \cdot \nabla_v F_{s0} \tag{5.2}$$

Where $\boldsymbol{E}$ and $\boldsymbol{B}$ are the perturbed electric and magnetic fields. Notice that the quantities in the equation refer to species s.

Under reasonable assumptions, the perturbation of the distribution function in 5.2 can be shown to take the form:

$$F_{s1}(\boldsymbol{r}, \boldsymbol{v}, t) = -\frac{q_s}{m_s} \int_{-\infty}^{t} [\boldsymbol{E}(\boldsymbol{r}', \boldsymbol{v}') + \boldsymbol{v}' \times \boldsymbol{B}(\boldsymbol{r}', t')] \cdot \nabla_v F_{s0}(\boldsymbol{v}') dt' \tag{5.3}$$

Where $(\boldsymbol{r}', \boldsymbol{v}')$ is the unperturbed trajectory which passes through the point $(\boldsymbol{r}, \boldsymbol{v})$ when $t' = t$.

Recalling now the Maxwell's equations in a medium, one can obtain the following relations:

$$\boldsymbol{k} \times \boldsymbol{E} = \omega \boldsymbol{B} \tag{5.4}$$

$$\boldsymbol{k} \times \boldsymbol{B} = -i\mu_0 \boldsymbol{j} - \frac{\omega}{c^2}\boldsymbol{E} = -\frac{\omega}{c^2}\boldsymbol{K} \cdot \boldsymbol{E} \tag{5.5}$$

Where $\boldsymbol{K}$ is the dielectric permittivity tensor. Carrying out some algebraic manipulations and writing the perturbed current $\boldsymbol{j}$ as in equation 2.15 yields the following important vector equation:

$$\boldsymbol{K} \cdot \boldsymbol{E} = \boldsymbol{E} + \frac{i}{\omega \varepsilon_0} \sum_s q_s \int \boldsymbol{v}\, F_{1s}\, d^3\boldsymbol{v} \tag{5.6}$$

Which, after linearization, translates in a linear system of equations whose unknowns are the amplitudes of the electric field components. In order to guarantee the existence of non-trivial solutions, the determinant must be equal to zero.

Assuming the equilibrium distribution function to be Maxwellian, imposing that the determinant is equal to zero leads - after many calculations - to the following expression for the dielectric permittivity tensor:

$$K_{ij} = \delta_{ij} + \sum_s \frac{\omega_{ps}^2}{\omega} \sqrt{\frac{m_s}{2T_s}} \frac{\exp(-\lambda_s)}{k_z} \sum_{n=-\infty}^{\infty} T_{ij} \tag{5.7}$$

Where δ_{ij} is Kronecker delta function, ω_{ps} is the plasma gyrofrequency of species s and T_{ij} is:

$$\begin{pmatrix} n^2\, I_n\, Z/\lambda_s & i\, n(I_n' - I_n)Z & -n\, I_n\, Z'/\sqrt{2\lambda_s} \\ -i\, n(I_n' - I_n)Z & (n^2\, I_n/\lambda_s + 2\lambda_s I_n - 2\lambda_s I_n')Z & i\sqrt{\lambda_s}(I_n' - I_n)Z'/\sqrt{2} \\ -n\, I_n\, Z'/\sqrt{2\lambda_s} & -i\sqrt{\lambda_s}(I_n' - I_n)Z'/\sqrt{2} & -I_n Z' \xi_n \end{pmatrix} \tag{5.8}$$

The above matrix makes use of some modified Bessel functions I_n with argument λ_s:

$$\lambda_s = \frac{T_s k_\perp^2}{m_s \omega_{cs}^2} \tag{5.9}$$

And of the plasma dispersion function Z along with its derivative Z', both with argument:

$$\xi_n = \frac{\omega - n\omega_{cs}}{k_z} \sqrt{\frac{m_s}{2T_s}} \tag{5.10}$$

Where ω_{cs} is the cyclotron frequency of species s.

Given that, equation 5.7 can be solved numerically to obtain the dispersion relation, in a linear nonrelativistic regime, for waves propagating in warm, magnetized plasmas.

A numerical solver of this kind will be used throughout the following study and will be often compared to PIC simulation results which, as will be exposed in the next section, on the other hand account for both relativistic and nonlinear effects.

5.2 Particle-in-cell methods

A comprehensive review on plasma simulations can be find in [36], where the Particle-in-cell concept and model is presented.

Generally speaking, Particle-in-cell (or PIC) methods are a family of computational methods whose aim is to simulate the plasma evolution in time while retaining nonlinear effects in the system (that is, from first principles).

Recalling section 2.1.3, which presented the Newton law of motion of a single particle when it is subject to the electromagnetic force, one could try to simulate a many-particle sistem such as a plasma by simply implementing a time-advancing method for the position $\boldsymbol{x}$ and velocity $\boldsymbol{v}$ of each particle and then updating the EM fields. This approach is usually referred to as the particle-particle (PP) method, which at each timestep solves the following set of equations for each particle:

$$\boldsymbol{x}_p^{i+1} = \boldsymbol{x}_p^i + \Delta t\, \boldsymbol{v}_p^i \tag{5.11}$$

$$\boldsymbol{v}_p^{i+1} = \boldsymbol{v}_p^i + \Delta t\, \boldsymbol{F}_p^i \tag{5.12}$$

where the index i refers to the timestep, while p refers to the particles. If the system contains N particles, then the total force $\boldsymbol{F}_p^i$ acting on the p-th particle at the i-th timestep is the summation of all the contributions from the other $p-1$ particles:

$$\boldsymbol{F}_p^i = \sum_{q=1\ q\neq p}^{N} \boldsymbol{F}_{p\,q}^i \tag{5.13}$$

That is, the summation over all the forces that derives from the interaction between the p-th particle and every other particle. This summation is computationally tractable for simulating a relatively small number of particles (as may be appropriate for strongly coupled systems), but is unfeasible for weakly coupled systems (where a large number of particles are present) such as the magnetospheric plasma.

Let us consider as an example the computation of the Coulomb force alone, which for a generic pair of particles with the same charge q has the following expression:

$$\boldsymbol{F}_{p\,q} = \frac{q^2}{4\pi\varepsilon_0} \frac{\boldsymbol{x}_q - \boldsymbol{x}_p}{|\boldsymbol{x}_q - \boldsymbol{x}_p|^3} \tag{5.14}$$

In the above equation particles are assumed to be points in space. The plot of such a force intensity, as a function of the distance $r = |\boldsymbol{x}_q - \boldsymbol{x}_p|$ between the particles, is shown in figure 5.2 (dashed line).

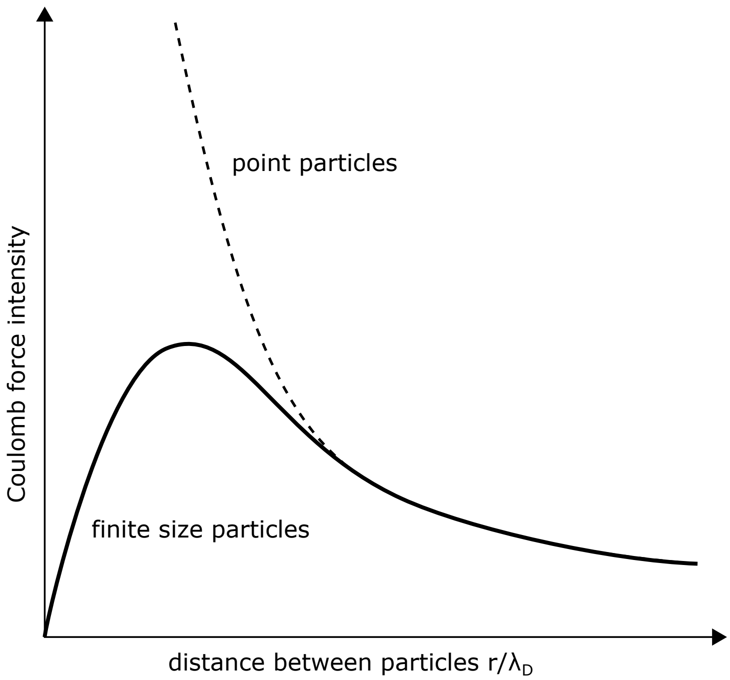

Figure 5.2: Qualitative depiction of two types of a Coulomb-like forces between a pair of particles, depending on the particle's nature. The dashed line represents the force between two point particles, while the solid line represents the force between two finite size particles.

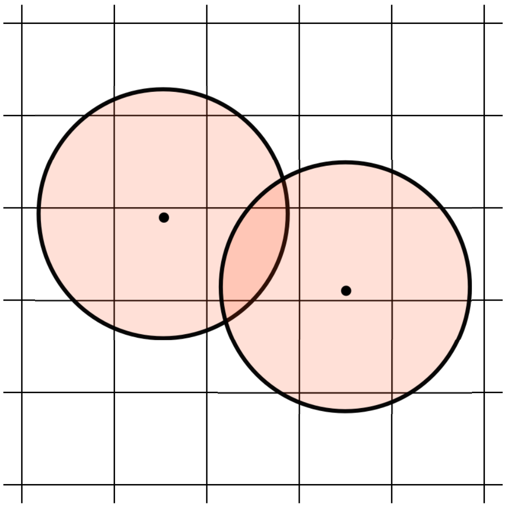

Figure 5.3: Qualitative example of finite size circular superparticles overlapping in a discrete computational grid, each one representing many physical particles.

Particle-in-cell methods rely on the so-called superparticles to reduce the computational weight and also to reduce the importance of collisional effects, which are represented by the rapid growth of the force intensity as $r \to 0$ and are significant in the case of point particles.

Superparticles represent a group of many physical particles. They move in a computational spatial grid. Their main feature is to be finite size particles: they can overlap (see figure 5.3) and, when they do, if their charges are equal and opposite it is assumed that inside the overlapping region they neutralize one another, thus transforming the Coulomb force depicted by the dashed line in figure 5.2 into the one depicted by the solid line in the same figure. When two superparticles completely overlap, the Coulomb force is of course equal to zero.

Finite size particles suit the simulation of plasmas because they correctly reproduce the collective behaviour of weakly coupled systems even if there are not as many computational particles as physical ones. This is because, as can be seen in figure 5.2, in the long range regime the behaviour of the Coulomb force stays the same as in the case of point particles.

PIC methods can account for relativistic effect or not, depending on how they compute the Lorentz force while advancing the position and velocity of particles.

5.3 Anisotropic Maxwell–Jüttner velocity distribution

In section 4.1.1 it was explained that an anisotropic velocity distribution could trigger the whistler instability. In that case the example of a bimaxwellian distribution, derived from a maxwellian one, was made.

However, as we shall see later, some of the simulations in this study show particle velocities close to relativistic regimes. This means that they will be more accurately modeled through an anisotropic velocity distribution based on the Maxwell–Jüttner distribution. For this reason, the simulations presented in this chapter were all carried out using an anisotropic Maxwell–Jüttner distribution.

The Maxwell–Jüttner distribution is, indeed, the relativistic analogue of the Maxwell distribution; it proves suitable in describing the velocities of particles moving with relativistic speed, in a ideal gas. In the limit of low temperatures ($T \ll m_0 c/k_B$ where m_0 is the rest mass of the particle) this distribution reduces to a maxwellian one.

A working example of an anisotropic Maxwell-Jüttner distribution is presented by Gladd in [37]:

$$F(U_\perp, U_\parallel) = C \,\exp\left(-\frac{\sqrt{1 + U_\perp^2 + AU_\parallel^2}}{\epsilon_\perp}\right) \tag{5.15}$$

$$U_\perp = \frac{v_\perp}{c}\frac{1}{\sqrt{1 - v_\perp^2/c^2}} \qquad U_\parallel = \frac{v_\parallel}{c}\frac{1}{\sqrt{1 - v_\parallel^2/c^2}} \tag{5.16}$$

$$C = \frac{\sqrt{A}}{4\pi\epsilon_\perp c^3 K_2(1/\epsilon_\perp)} \tag{5.17}$$

$$\epsilon_\perp = \frac{T_\perp}{m_{e0}\, c^2} \tag{5.18}$$

Where $U_\parallel$ and $U_\perp$ are the relativistic momenta, and K_2 is a second-order Bessel function of the second kind. The distribution becomes bimaxwellian when $\epsilon_\perp \ll 1$ [37].

Figure 5.4 shows the initial ($t\omega_{ce} = 0$) anisotropic Maxwell–Jüttner as generated by VPIC, in a case with $A = 5$, $\beta_\parallel = 0.15$ and $\omega_{pe}/\omega_{ce} = 2.1384$.

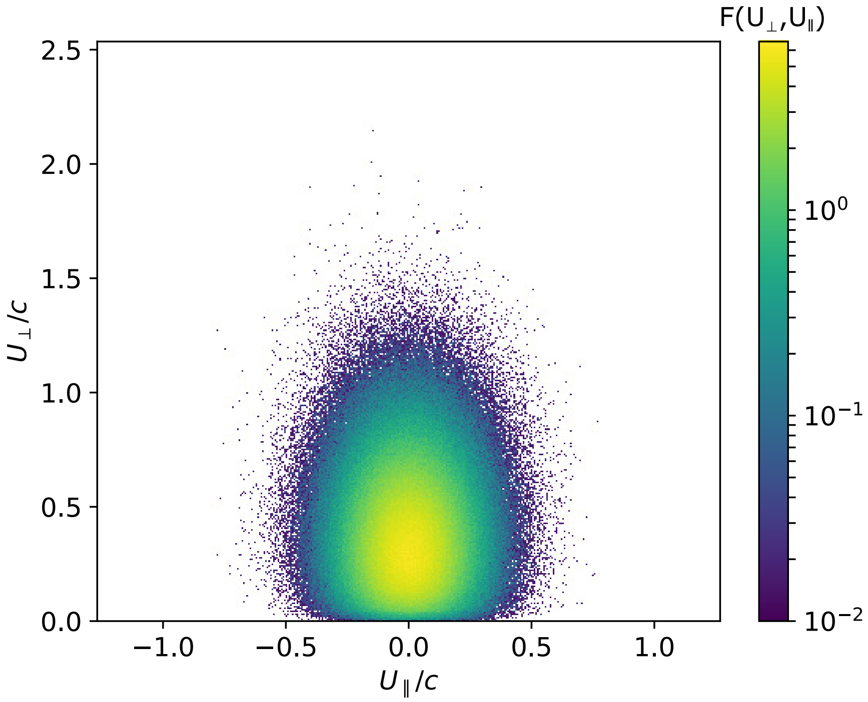

Figure 5.4: Initial ($t\omega_{ce} = 0$) Maxwell–Jüttner distribution for the relativistic momenta of particles, in cylindrical coordinates, when $A = 5$, $\beta_{\parallel} = 0.15$ and $\omega_{pe}/\omega_{ce} = 2.1384$.

5.4 The linear theory of Kennel and Petschek

In [22] Kennel and Petschek developed a method to compute an analytical expression for the whistler growth rate, given some approximations, starting from the Vlasov-Maxwell non-relativistic kinetic equations.

In order to explore the possibility of an analytical comparison, the Kennel-Petschek approximation was tested against VPIC and a linear solver of the linearized Vlasov-Maxwell equations: the results are exposed in this section.

They made the key assumption that $\gamma/\omega_R \ll 1$.

The resulting analytical expression for γ is the following:

$$\gamma = \pi\omega_{ce}\left(1-\frac{\omega}{\omega_{ce}}\right)^2 \eta\left(A-\frac{1}{\omega_{ce}/\omega-1}\right) \tag{5.19}$$

Where:

$$\eta = 2\pi\frac{\omega_{ce}-\omega}{k}\int_0^\infty v_\perp dv_\perp F(v_\perp, v_\parallel = V_R) \tag{5.20}$$

$$A = \left[\frac{1}{2\int_0^\infty v_\perp dv_\perp F}\int_0^\infty v_\perp dv_\perp\left(v_\parallel\frac{\partial F}{\partial v_\perp}-v_\perp\frac{\partial F}{\partial v_\parallel}\right)\frac{v_\perp}{v_\parallel}\right]\Bigg|_{v_\parallel=V_R} \tag{5.21}$$

$F(v_\perp,\, v_\parallel)$ is the velocity distribution function, which in the present case will be bimaxwellian (see equation 4.1).

Lastly, one has the resonant velocity for electrons defined as (for non-relativistic velocities):

$$V_R = \frac{\omega-\omega_{ce}}{k} \tag{5.22}$$

It is assumed that, in order to keep the growth rate low, the wave has a frequency such that only a small fraction of electrons is resonant with it.

Carrying out the calculations with the bimaxwellian distribution, equations 5.20 and 5.21 reduce to:

$$\eta = \frac{1}{\sqrt{2\pi}}\frac{\omega_{ce}-\omega}{k\theta_\parallel}\exp\left[-\frac{1}{2}\left(\frac{\omega_{ce}-\omega}{k\theta_\parallel}\right)^2\right] \tag{5.23}$$

$$A = \frac{\theta_\perp^2-\theta_\parallel^2}{\theta_\parallel^2} \tag{5.24}$$

Now, these results will be plugged into equation 5.19 and physical quantities will be made adimensional sticking to the following normalization rule:

$$x = \frac{ck}{\omega_{pe}} \qquad y = \frac{\omega}{\omega_{ce}} \tag{5.25}$$

The resulting normalized expression for γ is:

$$\frac{\gamma(x,y)}{\omega_{ce}} = c\sqrt{\frac{\pi}{2}}\frac{(1-y)^3}{\alpha\, x\, \theta_\parallel}\left(A - \frac{y}{1-y}\right)\exp\left[-\frac{c^2}{2}\frac{(1-y)^2}{\alpha^2\, x^2\, \theta_\parallel^2}\right] \tag{5.26}$$

γ will become a function of solely the wavenumber once the whistler dispersion relation is be used to relate y to x.

The accuracy of the approximation is shown in figure 5.5. Indeed, the figure shows the growth rate obtained by the Kennel and Petschek theory and compares it against the linear solver and non-linear VPIC simulations. Overall the range of unstable modes is the same but the Kennel and Petschek theory overestimates the maximum growth rate by a factor of ~ 2 due to its approximations.

The chosen test case was:

$$A = 5 \qquad \omega_{pe}/\omega_{ce} = 2.1384 \qquad \beta_\parallel = 0.04$$

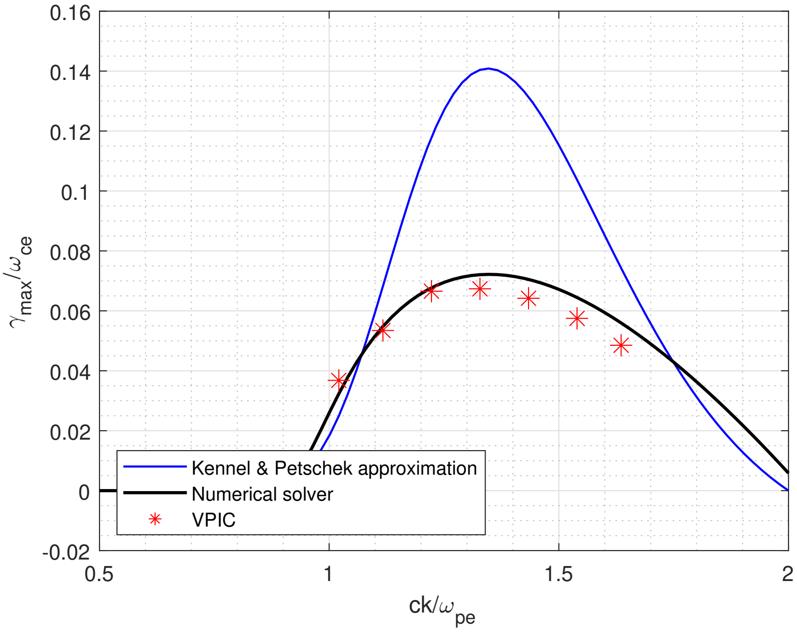

Figure 5.5: Comparison of the growth rates of the whistler instability obtained from Kennel and Petschek theory, a numerical linear solver and nonlinear VPIC simulations.

5.5 Physical and numerical setup

5.5.1 Plasma composition

The subject of the study will be the whistler instability as it develops in a plasma subject to an external magnetic field $\boldsymbol{B}_0$ and composed of the following species:

- **Warm electrons** with an anisotropic Maxwell–Jüttner velocity distribution and an initial temperature anisotropy $A = T_\perp / T_\parallel$.
- **Cold electrons** which represent a varying fraction of the total electron population (from 0 to 0.9), with a maxwellian velocity distribution and a temperature $T_c = T_\parallel / 100$.
- **Ions** with a maxwellian velocity distribution and a temperature $T_i = T_c$ and density equal to the total electron density.

For the parameters considered, the maximum growth rate always occurs at parallel propagation (see section 4.3).

5.5.2 Relevant parameters

As can be inferred from chapter 4 the parameters that affect the instability, and therefore need to be varied parametrically, are:

- **Parallel, warm ratio of plasma pressure to magnetic pressure** $\beta_\parallel$ which, in order to ensure parallel propagation, must be above a critical value $\beta_\parallel^*$ that depends on the density of cold electrons.
  The presence of cold electrons makes the value of $\beta_\parallel^*$ decrease, so the study will use values of $\beta_\parallel$ that are above the reference $\beta_{\parallel 0}^* = 0.0245$ which is the critical value corresponding to zero cold electron density.
- **Density of the cold population relative to the total electron density** n_c/n_e which will vary between 0.0 and 0.9.
- **The initial temperature anisotropy** $A = T_\perp / T_\parallel$ of the warm population, which initially triggers the instability and affects how quickly it grows. Its value must be higher than 1 [22]. Furthermore, in order to obtain accurate results from PIC simulations, high enough values of this parameter must be used. This is because PIC codes suffer from statistical noise coming from the finite number of superparticles and small growth rates are hard to obtain accurately with the PIC technique.

5.5.3 Environmental conditions

Some fixed quantities were chosen in order to reproduce the environmental conditions found by the Van Allen Probes observations [38] in the magnetosphere. The external, constant magnetic field was:

$$|\boldsymbol{B}_0| = 150 \text{ nT} \tag{5.27}$$

The warm electron density was kept constant too:

$$n_h = 10^6 \text{ m}^{-3} \tag{5.28}$$

This means that the total electron density, computed as:

$$n_e = n_h + n_c \tag{5.29}$$

may vary between simulations as a consequence of the variation of the cold electron density n_c. In physical units, the cold electron density is varied between 0 and 100 cm^{-3}, as representative of the region of near-Earth space near the plasmapause.

Combining the above values for $|\boldsymbol{B}_0|$ and n_e, the following reference value of ω_{pe}/ω_{ce} was computed in the absence of cold electrons (when $n_h = n_e$):

$$\frac{\omega_{pe}}{\omega_{ce}} \approx 2.1384 \tag{5.30}$$

5.5.4 Numerical setup

The simulations presented in this chapter were carried out over a domain shaped like the one in figure 5.6. Since three species (and hence three electron temperatures) are usually present, the reference Debye length λ_D for each simulation was computed using the smallest one.

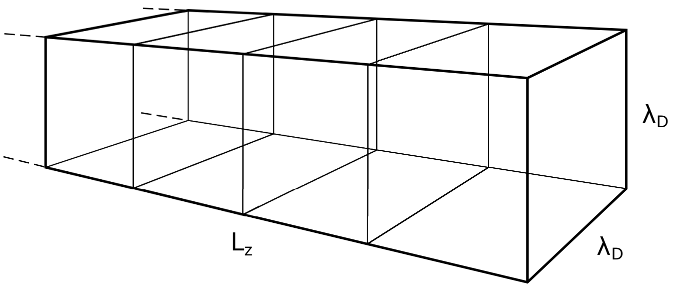

Figure 5.6: VPIC is a three-dimensional code, but the computational domain was shaped as to reproduce a one-dimensional layout by imposing $L_x = L_y = \lambda_D$. L_z is always equal to $20\, c/\omega_{pe}$.

The length of the domain in the dimension of interest was $L_z = 20\,c/\omega_{pe}$. This value was chosen after several attempts with shorter domains, which showed that the excitation of different modes depending on the domain length influenced the growth rate and regime behaviour of the magnetic field, thus making those simulations unrealiable.

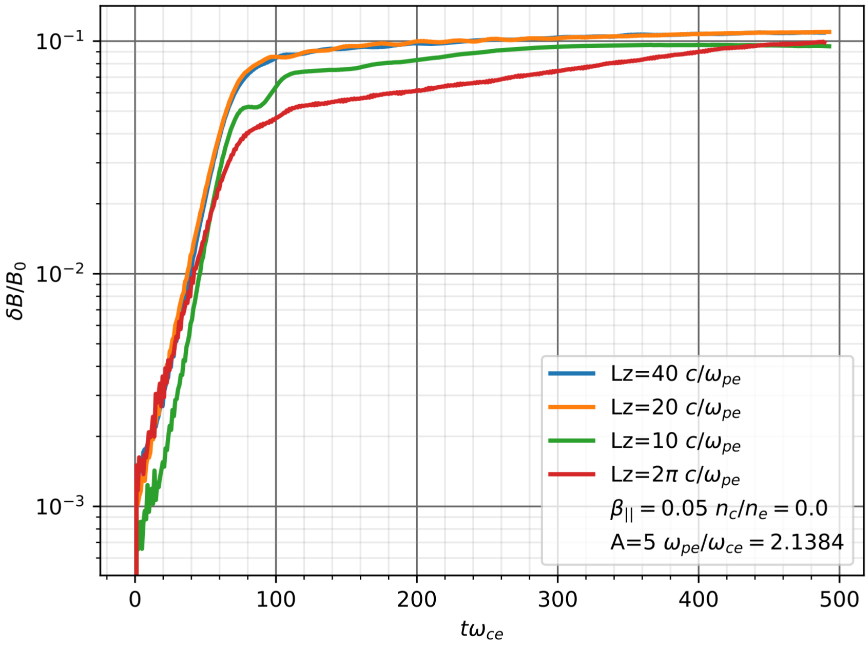

Figure 5.7: When no cold electrons are present in the system, $L_z = 10\,c/\omega_{pe}$ is sufficient to capture the saturation amplitude of the whistler waves.

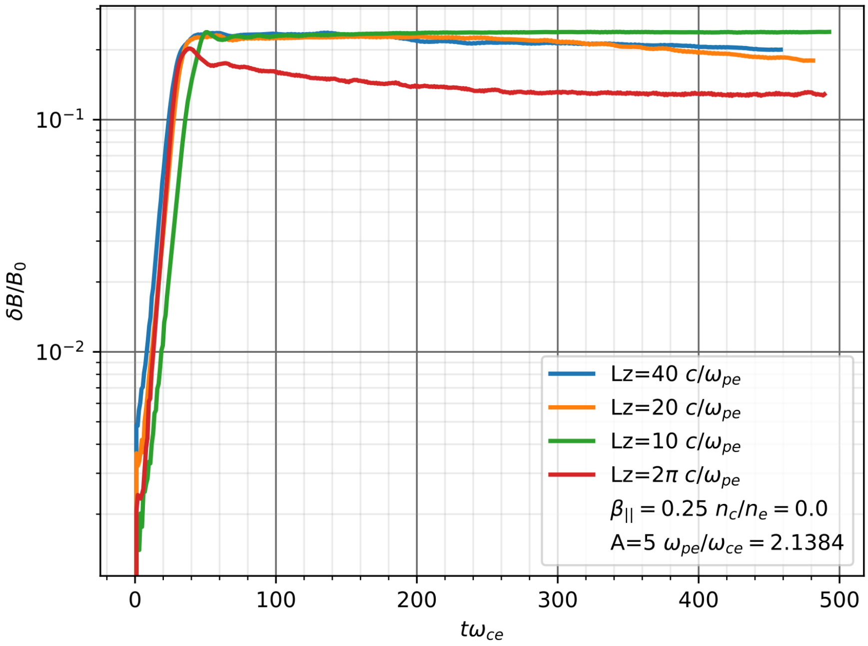

Figure 5.8: When no cold electrons are present in the system, $L_z = 10\,c/\omega_{pe}$ is sufficient to capture the saturation amplitude of the whistler waves.

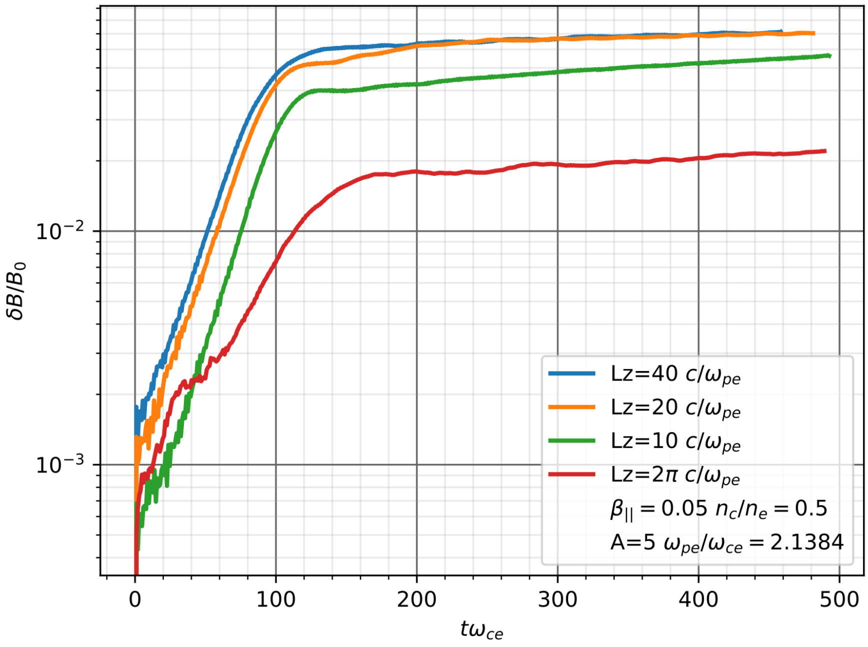

Figure 5.9: With cold electrons, $L_z = 20\,c/\omega_{pe}$ is sufficient to capture the saturation amplitude of the whistler waves accurately.

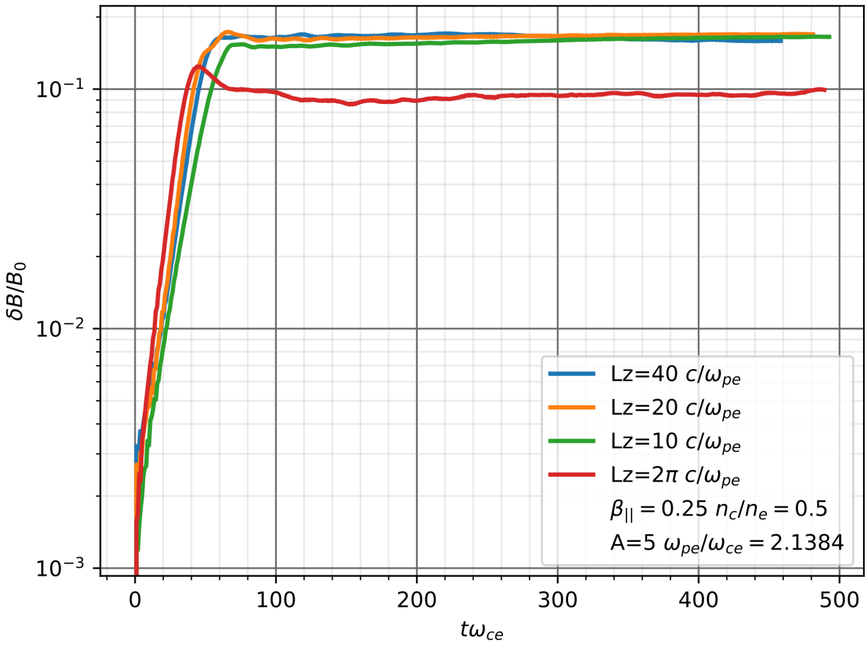

Figure 5.10: With cold electrons, $L_z = 20\,c/\omega_{pe}$ is sufficient to capture the saturation amplitude of the whistler waves accurately.

The number of cells n_z for each simulation was chosen so that:

$$L_z/n_z \approx \lambda_D \tag{5.31}$$

In order to maintain good spatial resolution.

The timestep for each simulation was chosen as to satisfy the Courant-Friedrichs-Lewy condition. Periodic boundary conditions for both particles and fields were applied. The number of particles per cell *nppc* was equal to 4000 for every run.

5.6 Preliminary study with nonrelativistic linear theory

5.6.1 Agreement between the linear solver and VPIC

In order to assess the agreement between the linear solver of the linearized Vlasov-Maxwell equations (chapter 11 of [35]) and VPIC, some preliminary tests were carried out.

Results are presented for the following physical setup:

$$A = 5 \qquad \omega_{pe}/\omega_{ce} = 2.1384 \qquad \beta_{\|} = 0.04 \qquad n_c/n_e = 0.0$$

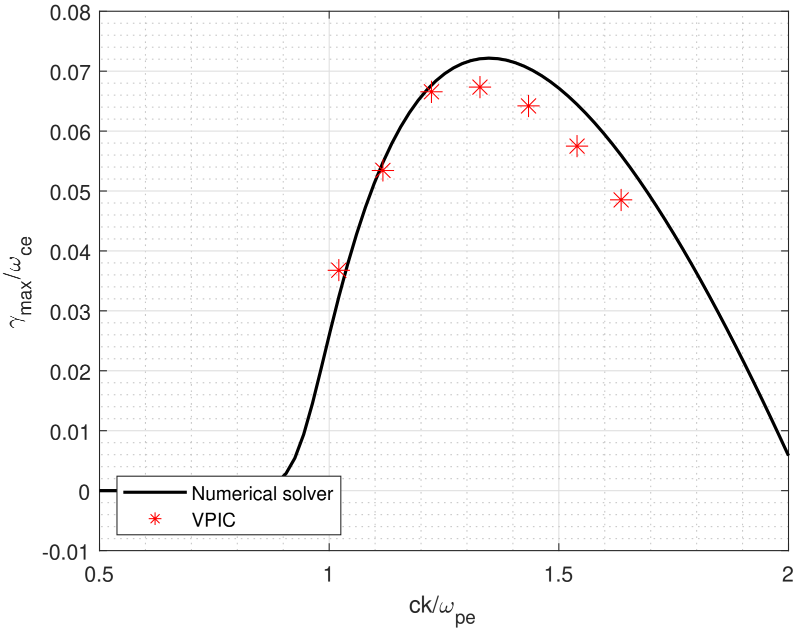

Figure 5.11: Comparison between the linear solver and VPIC in a test case.

5.6.2 Overview of the parameter space

Here a preliminary study of the chosen parameter space is presented. It was carried out with the linear solver of the linearized Vlasov-Maxwell equations. It must be noted, for further considerations, that the solver does not consider relativistic effects associated with the velocity of the particles and so it is used here just to get some guidance on the parameters that should be most interesting to explore.

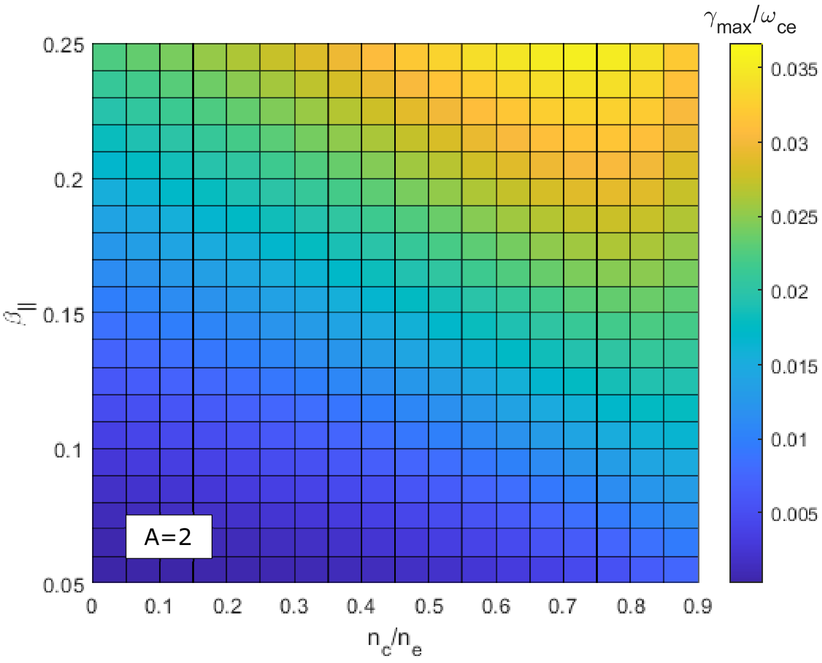

Figure 5.12: Maximum growth rate for $A = 2$, varying $\beta_{\|}$ and n_c/n_e.

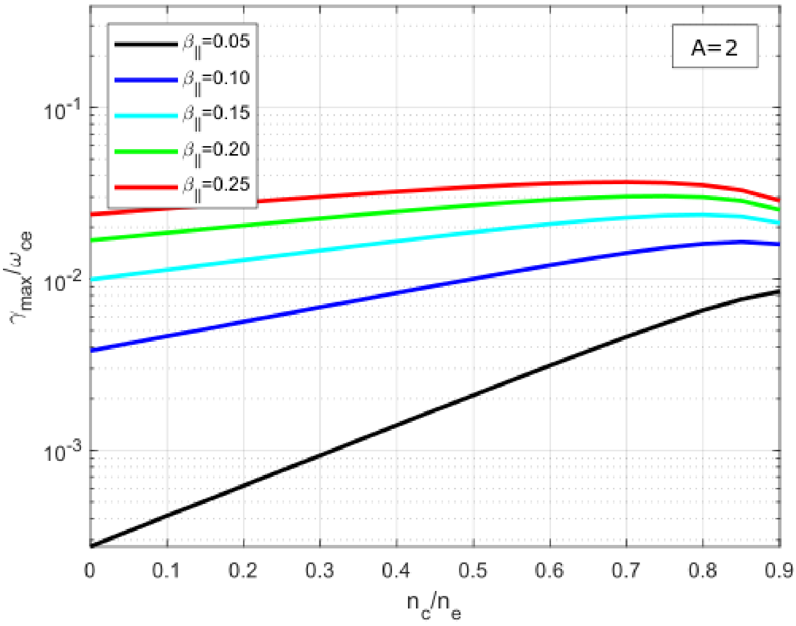

Figure 5.13: Results of 5.12 presented for different values of $\beta_{\|}$. The growth rate appears to steadily increase as a function of n_c/n_e up to $n_c/n_e \sim 0.8$ as observed in [30].

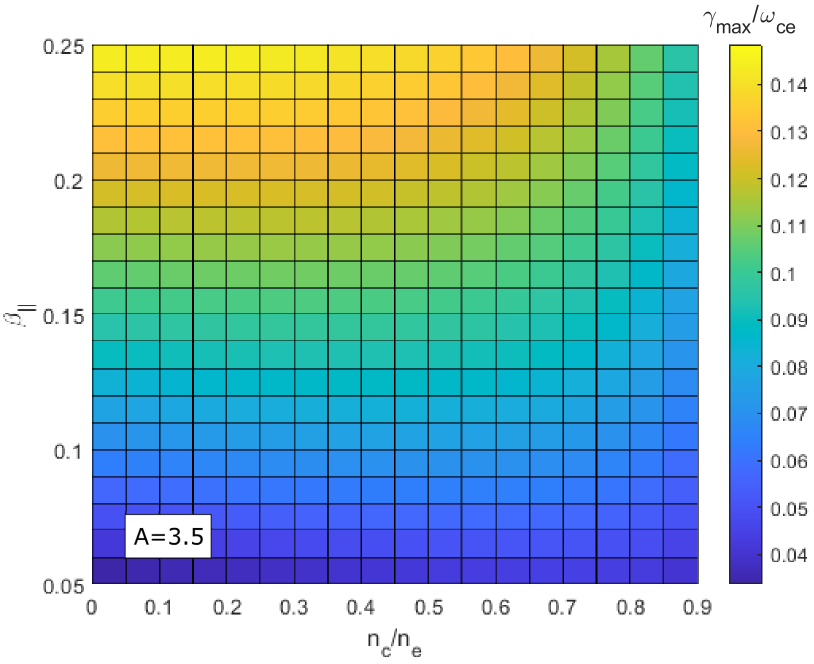

Figure 5.14: Maximum growth rate for $A = 3.5$, varying $\beta_{||}$ and n_c/n_e.

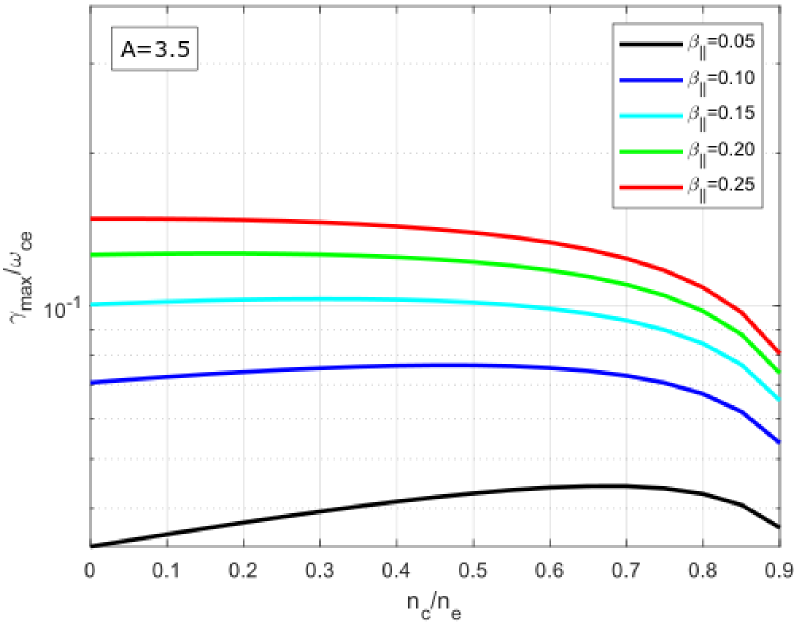

Figure 5.15: Results of 5.14 presented for different values of $\beta_{||}$. The critical value of n_c/n_e appears to have shifted to the left.

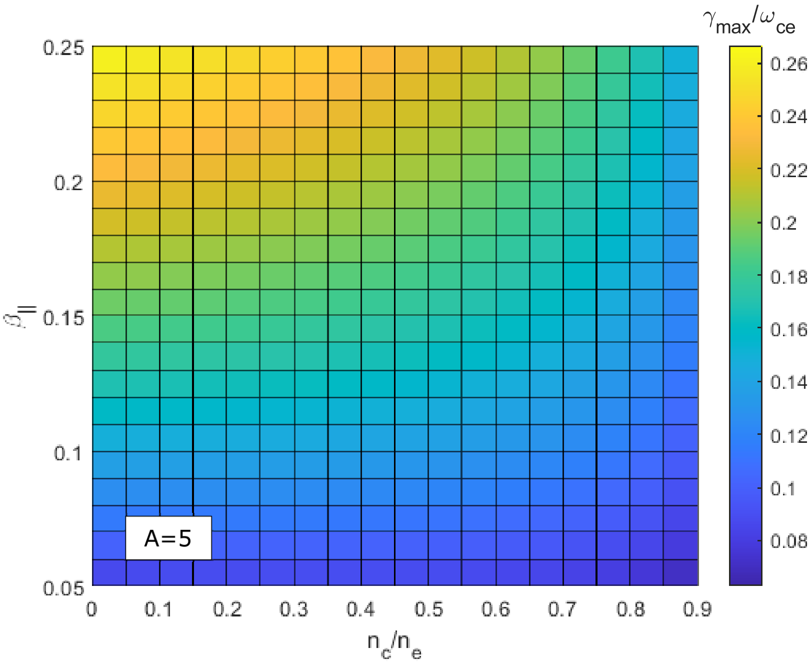

Figure 5.16: Maximum growth rate for $A = 5$, varying $\beta_\parallel$ and n_c/n_e.

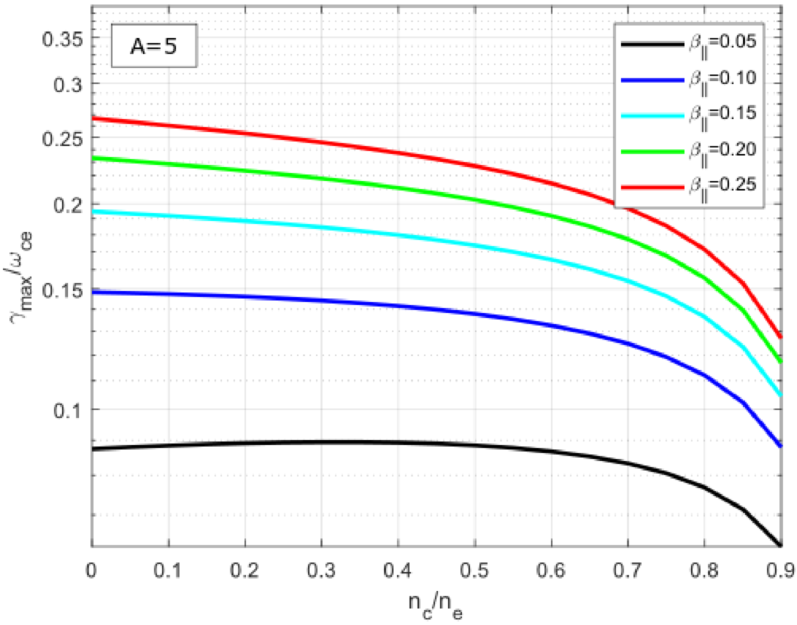

Figure 5.17: Results of 5.16 presented for different values of $\beta_\parallel$. For most values of $\beta_\parallel$ the growth rate has its peaks at $n_c/n_e = 0$ and then decreases monotonically.

From figures 5.12-5.17 it appears that the maximum growth rate has a peak, while increasing the cold electron density, whose position tends to $n_c/n_e = 0.0$ as the anisotropy of the warm electrons increases.

Despite even lower values of anisotropy may be of interest, in the next sections it will be shown that VPIC was used to study only the case in which $A = 5$. This is because, as already explained, PIC simulations struggle in reproducing low values of anisotropy.

5.7 Relativistic effects

Despite the good agreement between the linear solver and VPIC that was shown in figure 5.11, it is apparent that results from VPIC do not match exactly the ones from the solver. This discrepancy is more and more evident with increasing $\beta_{\|}$, which means - in a setup that keeps ω_{pe}/ω_{ce} fixed - increasing the warm electron velocity, as seen in figure 5.18.

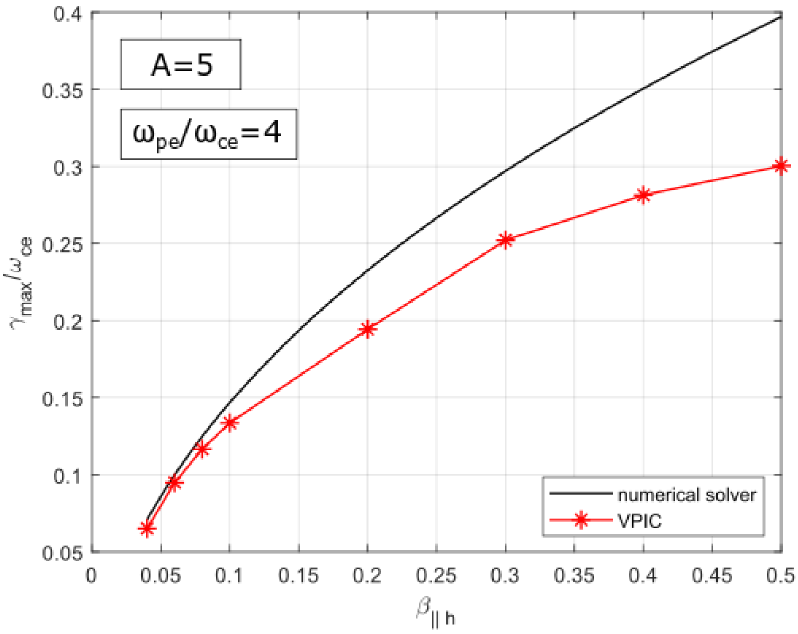

Figure 5.18: Discrepancy between the linear solver and VPIC for increasing thermal velocities, in logarithmic scale.

These observations likely lead to the conclusion that, when velocities are above $\sim 0.15c$, relativistic effects kick in and influence the growth rate. The same conclusion was reached by Gladd [37]. It must be reminded that VPIC is a relativistic code, while the linear solver does not take into account relativistic effects.

Some testing was made against the results presented by Gladd in [37]. Defining $\varepsilon_{\perp}$ as:

$$\varepsilon_{\perp} = \frac{T_{\perp h}}{m_e c^2} \tag{5.32}$$

The following three testing setups were considered, which show increasing perpendicular warm temperature and velocity:

Setup 1: $A = 5$ $\omega_{pe}/\omega_{ce} = 2.7385$ $\varepsilon_{\perp} = 0.02$
Setup 2: $A = 5$ $\omega_{pe}/\omega_{ce} = 1.3283$ $\varepsilon_{\perp} = 0.10$

$$\textbf{Setup 3:}\ A = 5 \qquad \omega_{pe}/\omega_{ce} = 0.8660 \qquad \varepsilon_{\perp} = 0.20$$

Table 5.1 sums up the results obtained for the maximum growth rate. Table 5.1 confirms that when the thermal velocities are lower VPIC, the linear solver and Gladd's theory agree pretty well. As the thermal velocities are increased, there is a progressive departure of VPIC and Gladd's theory relative to the linear solver. On the other hand, Gladd's theory and VPIC remain in good agreement. This is the confirmation that, as the thermal velocities of the plasma increase, relativistic effects come into play.

	Gladd (1983)	**linear solver**	**VPIC (anisotropic Jüttner)**
Setup 1	≈0.093	0.10061	0.09118
Setup 2	≈0.063	0.10511	0.05842
Setup 3	≈0.031	0.10873	0.02977

Table 5.1: Values of γ_{max}/ω_{ce}

Also, table 5.2 shows the results from a test case with nonrelativistic velocities:

$$\omega_{pe}/\omega_{ce} = 4.0 \qquad \beta_{\|} = 0.01283 \qquad A = 5.0$$

Results highlight the fact that, in a nonrelativistic regime, the anisotropic Maxwell–Jüttner distribution does not behave much differently from a bimaxwellian one - and both simulations agree with the linear solver.

linear solver	**VPIC (bimaxwellian)**	**VPIC (anisotropic Jüttner)**
0.01997	0.02079	0.02034

Table 5.2: Values of γ_{max}/ω_{ce}

5.8 Simulation of the effects of the cold electrons density

The following section will present plots that show results from both the linear solver and VPIC simulations. The aim is to study the effects of increasing cold electrons density on two quantities: the maximum growth rate of the instability γ_{max}/ω_{ce} and the saturation value of the magnetic perturbation $\delta B/B_0$.

5.8.1 Effect on the maximum growth rate

It was found in [30] through nonrelativistic linear theory analysis that, at least in some conditions (for example, $\beta_\parallel = 0.1$ and $A = 1.822$ as well as $A = 2.244$), the addition of cold electrons while keeping the warm density fixed leads to an increase of the growth rate, which reaches a peak around $n_c/n_e \sim 0.8$ and then starts decreasing. This agrees with figure 5.12, whose results could however not be reproduced in VPIC since the anisotropy was too low.

However, both the linear solver and VPIC simulations (see figures 5.19, 5.20 and 5.21) agree on the fact that, at least for $A = 5$ and for the higher values of $\beta_\parallel$, increasing cold electrons density - while keeping the warm electrons density constant, as explained in section 5.5.3 - causes the maximum growth rate to decrease.

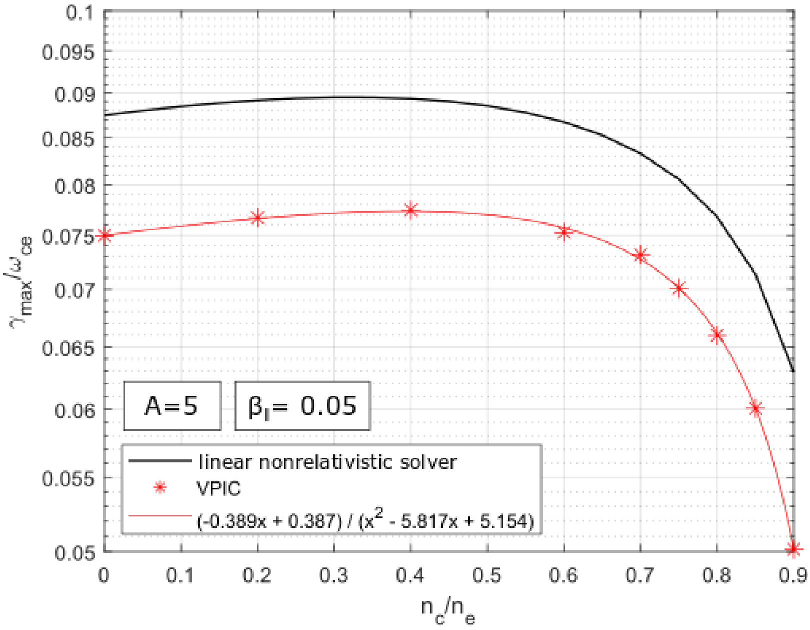

Figure 5.19: $\beta_\parallel = 0.05$ - The maximum growth rate slightly increases with increasing n_c/n_e up to $n_c/n_e \sim 0.5$ and then starts decreasing.

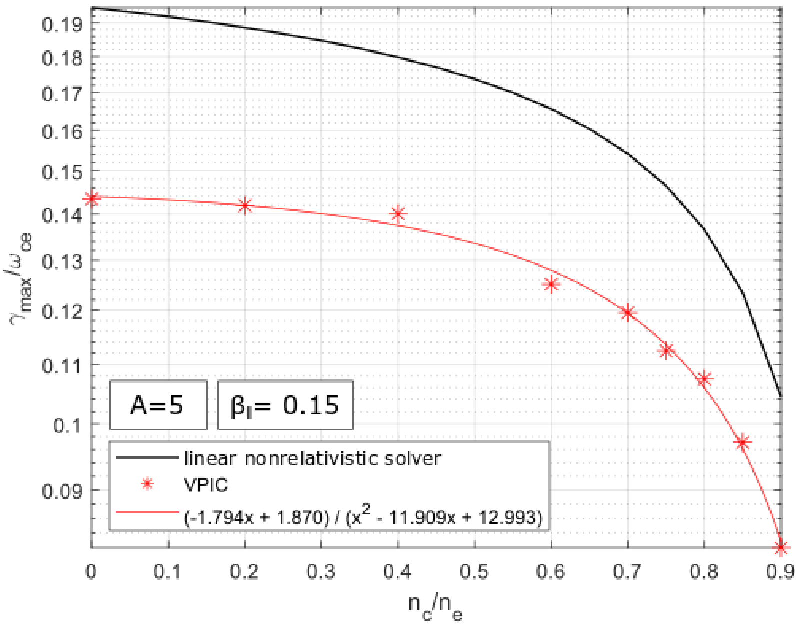

Figure 5.20: $\beta_{\|} = 0.15$ - The maximum growth rate decreases with increasing cold electrons.

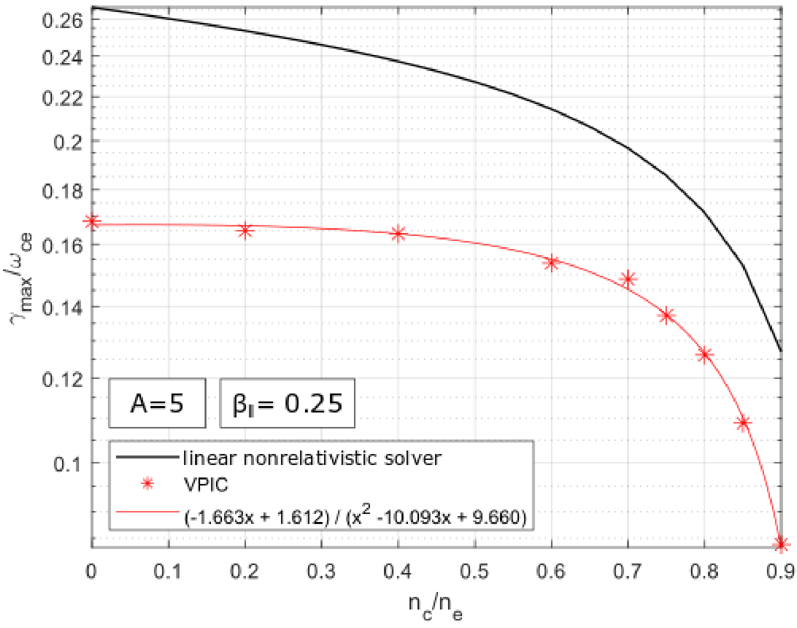

Figure 5.21: $\beta_{\|} = 0.25$ - Again, the maximum growth rate decreases with increasing cold electrons.

Results in figures 5.19, 5.20 and 5.21 differ only for the fact that they where obtained for increasing values of $\beta_{\|}$ - which are 0.05, 0.15 and 0.25. It can be noticed that, as expected from figure 5.18, the initial discrepancy at $n_c/n_e = 0.0$ between the linear solver and VPIC increases with $\beta_{\|}$ due to relativistic effects that the linear solver does not account for and that, on the other hand, are present in the PIC code.

In this section, there are two main conclusions: firstly, the relativistic effects decrease the growth rate, by values up to $30-40\%$ for the parameters considered; secondly, the cold electron density has a relatively small effect on the growth rate up to $n_c/n_e \sim 0.5$ but it has a strongly stabilizing effect for larger values of n_c/n_e.

5.8.2 Effect on the saturation amplitude of the whistler waves

Two approaches were tested in the extrapolation of the magnetic perturbation $\delta B/B_0$ saturation value (both are shown in figure 5.22):

- The first approach tried to reproduce the one used in [23] and consisted in taking the "knee value", right after the end of the linear growth phase, which was chosen as the value of $\delta B/B_0$ reached when the linear growth rate has become 20% of its former value during the initial growth.
- The second approach consisted in taking the asymptotic value of $\delta B/B_0$, which was usually reached after a longer time and was greater than the knee value.

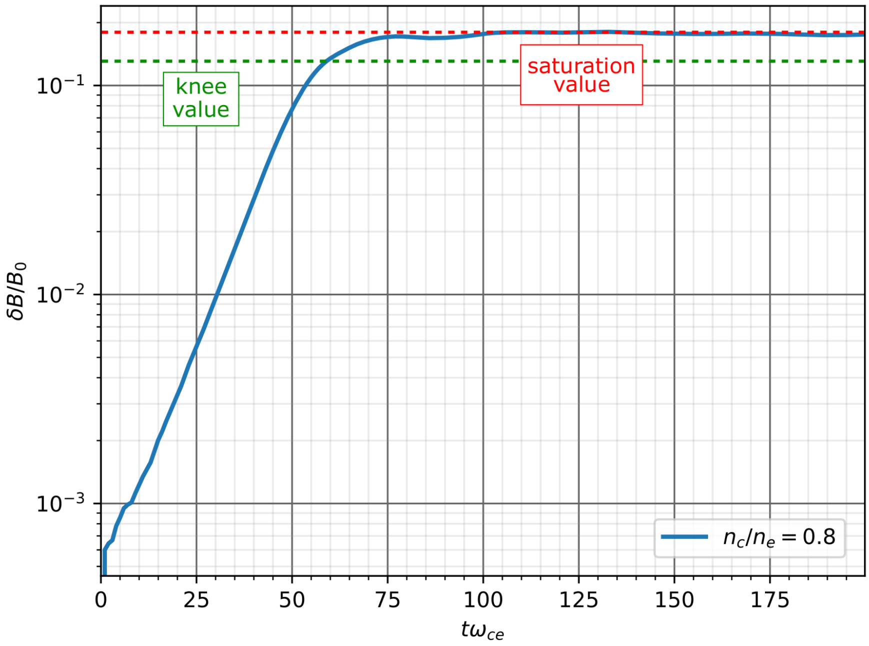

Figure 5.22: Different approaches tested in taking the final amplitude of $\delta B/B_0$. The knee value corresponds to a point where the growth rate has become 20% of its former value during the initial growth.

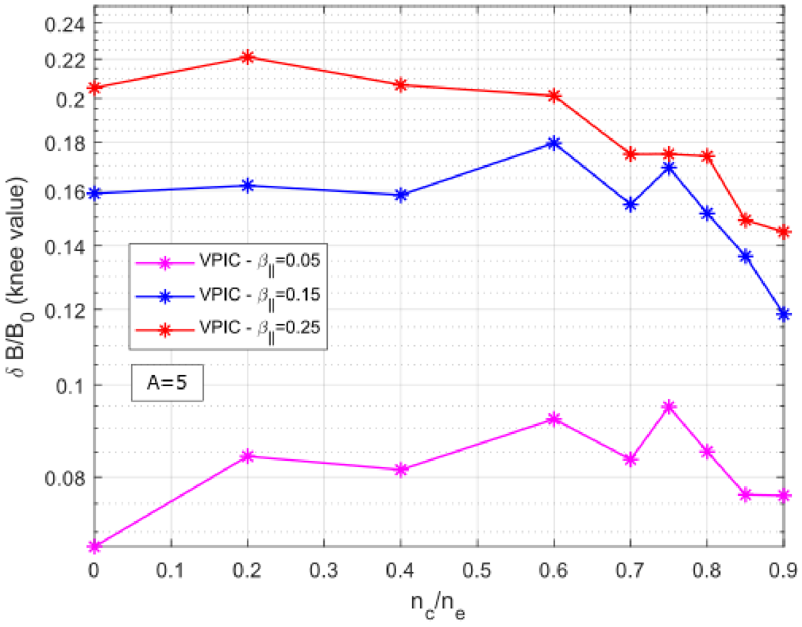

Figure 5.23: $\delta B/B_0$ as a function of n_c/n_e using approach number one: the plots are difficult to read and not suitable for fitting.

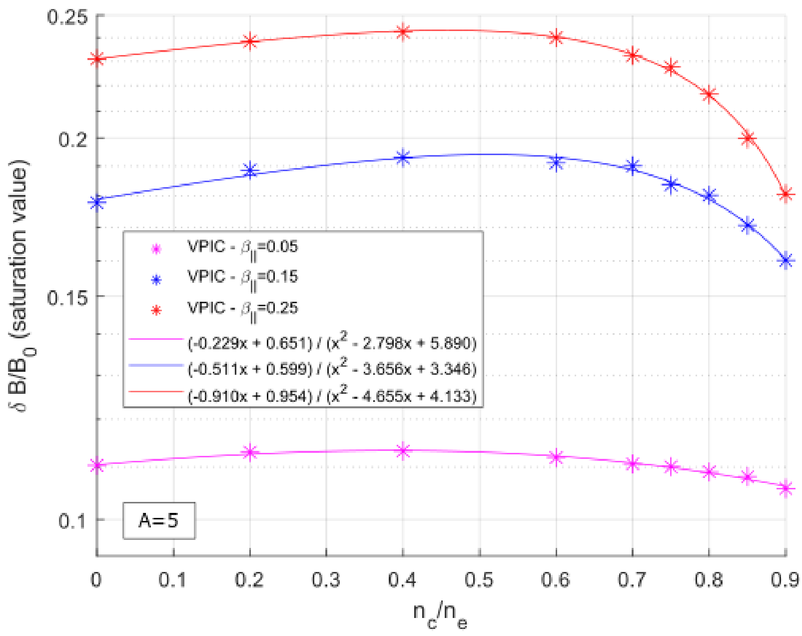

Figure 5.24: $\delta B/B_0$ as a function of n_c/n_e using approach number two: the plots were fitted with rational polynomials.

Figures 5.23 and 5.24 show results obtained with the two approaches described above. Approach number two appears to produce smoother results that nicely follow a fit with equation 5.33, with coefficients that are reported in table 5.3.

$$y = \frac{\mathrm{a}\,x + \mathrm{b}}{x^2 + \mathrm{c}\,x + \mathrm{d}} \tag{5.33}$$

	a	b	c	d
$\beta_\parallel = 0.05$	-0.229	0.651	-2.798	5.890
$\beta_\parallel = 0.15$	-0.511	0.599	-3.656	3.346
$\beta_\parallel = 0.25$	-0.910	0.954	-4.655	4.133

Table 5.3: Coefficients of the fit based on equation 5.33 for all the three values of $\beta_\parallel$ that were used during simulations. The fit curves are shown, along with experimental data, in figure 5.24.

The important conclusion is that the effect of increasing cold population on the saturation value of $\delta B/B_0$, while keeping the warm electrons density constant, appears to be marginal if not for high values of $\beta_\parallel$. As expected [38] the evolution of $\delta B/B_0$ over increasing n_c/n_e follows that of the growth rate in figures 5.19, 5.20 and 5.21, where data were also fitted with rational polynomials.

5.9 Scaling law for the magnetic perturbation

This last section will present an analysis similar to those in [23] regarding the behaviour, in the absence of cold electrons, of the saturated whistler wave amplitude $\delta B/B_0$ over increasing $\beta_{\|}$ for the warm electrons. Indeed, it was suggested in [23] that the scaling law between $\delta B/B_0$ and $\beta_{\|}$ might be linear.

The aim is to evaluate two different scaling laws for the saturated $\delta B/B_0$ (extrapolated using approach number two of the previous section - that is, taking the asymptotic value of the saturated curve), namely a linear function and a quadratic function.

The coefficient of determination R^2 was computed with Matlab functions and, for both the linear and quadratic fit, it was found very close to 1 (slightly better for the quadratic fit than for the linear one). Although the quadratic fit appears a bit better, over the range of parameters considered the linear fit (consistent with the results of [23]) is also a good approximation to the saturation amplitude.

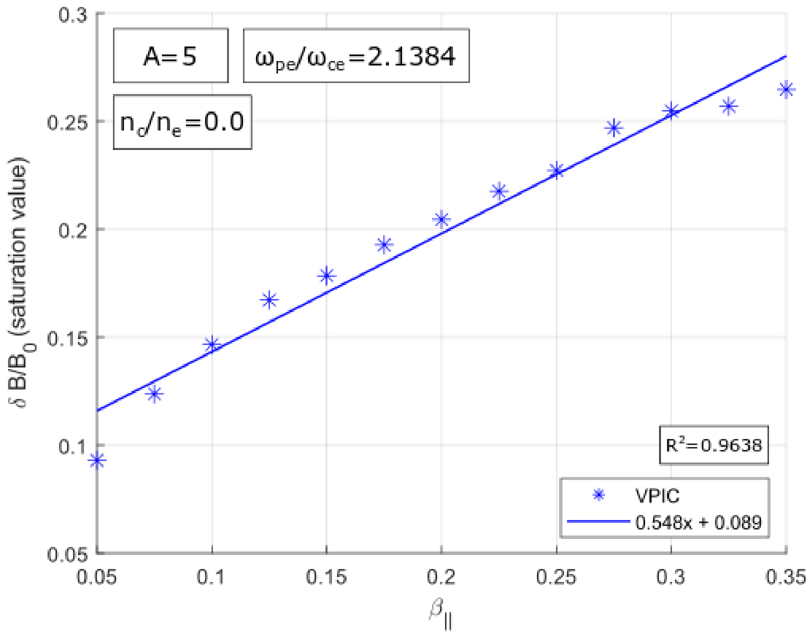

Figure 5.25: Saturated values of $\delta B/B_0$ taken as shown by the red line in figure 5.22. All the simulations were carried out with no cold electrons. Linear scaling law used to fit the data.

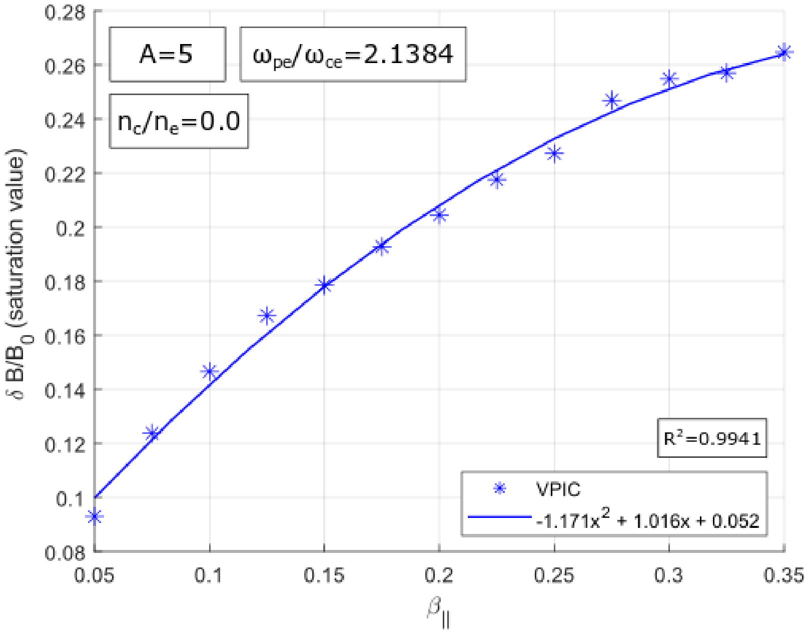

Figure 5.26: Saturated values of $\delta B/B_0$ taken as shown by the red line in figure 5.22. All the simulations were carried out with no cold electrons. Quadratic scaling law used to fit the data.

Conclusions

Whistler waves play a major role in the dynamics of the Earth's magnetosphere. They can interact effectively with the energetic particles present in the magnetosphere, inducing transport, acceleration and losses of those particles. Thus, whistler waves (and other waves (such as electromagnetic ion-cyclotron waves) play an important role in regulating the dynamics of the ring current, plasma-sheet and radiation belts, all of which are critical players in the inner magnetosphere dynamics.

In the Earth's magnetosphere, whistler waves can be generated by a kinetic (microscopic) instability, called the whistler instability, associated with the anisotropy of the energy distribution of warm electrons, with energies of the order of several kiloelectronvolts (keV). This is the main generation mechanism for the so-called whistler-mode chorus waves, which reside in the outer inner magnetosphere outside the plasmapause. The same instability can also contribute to generation of so-called whistler-mode hiss, which are broadband whistler mode waves residing primarily inside the plasmasphere and in plasmaspheric plumes.

In this Master's thesis we have studied the effect of an additional, cold (energy of the order of several eV) electron population on the whistler instability. Such cold electron population is very often present in the inner magnetosphere and has its origins in the Earth's ionosphere. It is known to affect the properties of the whistler waves, including frequency and growth rate, but its effect on the saturation amplitude of the waves has not been studied.

The present analysis has been conducted with two different tools. The first is a linear stability solver based on the kinetic, Vlasov-Maxwell equations in the non-relativistic regime. The second is a first-principle Particle-In-Cell code which solves the relativistic Vlasov-Maxwell equations and includes full non-linear effects. The comparison of the results obtained by these two methods allows one to understand the importance of relativistic and non-linear effects on the instability. Our primary contributions are three:

1. We have performed a detailed linear theory study, varying parametrically the parallell and perpendicular temperatures of the warm electrons that drive the

whistler instability (parameterized by the value $\beta_{\|}$ and the ratio between perpendicular and parallel temperatures A), and the density of the cold electrons. We found that the impact of the cold electrons on the maximum growth rate of the instability is small when the cold electrons carry up to $50-60\%$ of the total density. The impact of the cold electrons on the maximum growth rate is large when they carry most of the density, leading to strong stabilization. The linear theory results have been successfully benchmarked against the nonlinear PIC simulations when bi-Maxwellian distribution functions were used and the thermal velocity of the warm electrons was less than approximately 10% of the speed of light;

2. A comparison between the nonrelativistic linear solver and relativistic nonlinear PIC simulations revealed that relativistic effects can be very important for the development of the whistler instability and that in general they lead to a lower maximum growth rate. For the parameters considered, the reduction of the growth rate was about $30-40\%$;

3. We have performed non-linear PIC simulations of the instability. We have studied both the linear phase and the non-linear saturation. We have identified scaling laws of the saturated wave amplitudes versus background parameters. Specifically, in the case without cold electrons, we have reproduced the scaling law obtained by An et al. in [23] where the amplitude of the wave magnetic field scales proportionally to $\beta_{\|}$. Importantly, we have determined for the first time the scaling law of the magnetic perturbation versus the cold electron density:

$$y = \frac{\mathrm{a}\,x + \mathrm{b}}{x^2 + \mathrm{c}\,x + \mathrm{d}}$$

where y represents the magnetic perturbation $\delta B/B_0$, x represents the cold-to-total density ratio n_c/n_e and a, b, c, and d are coefficients that depends on the background plasma conditions.

These results are very important as they provide the first parametrization of the saturated magnetic field wave amplitude of the whistler waves generated by the whistler instability, including both relativistic effects and the effects of a cold electron population. This parametrization can be used in models of the inner magnetosphere (such as ring current models or radiation belt models) which typically only treat the waves empirically. It will yield for the first-time a physics-based treatment of the waves and a step forward towards the first-principle modeling and forecasting of the inner magnetosphere. A manuscript summarizing the results of this thesis is in preparation for one of the major space-physics international journals.

Calculus notation and vector identities

Newton's notation for differentiation

If y is a function of t:

$$\dot{y} = \frac{d\,y}{d\,t}$$

$$\ddot{y} = \frac{d^2\,y}{d\,t^2}$$

Calculus operators

Divergence	$\nabla \cdot \boldsymbol{F} = \frac{\partial F_x}{\partial x} + \frac{\partial F_y}{\partial y} + \frac{\partial F_z}{\partial z}$
Gradiend	$\nabla F = \left(\frac{\partial F}{\partial x}, \frac{\partial F}{\partial y}, \frac{\partial F}{\partial z} \right)$
Curl	$\nabla \times \boldsymbol{F} = \left(\frac{\partial F_z}{\partial y} - \frac{\partial F_y}{\partial z}, \frac{\partial F_x}{\partial z} - \frac{\partial F_z}{\partial x}, \frac{\partial F_y}{\partial x} - \frac{\partial F_x}{\partial y} \right)$
Laplacian	$\nabla^2 F = \frac{\partial^2 F}{\partial x^2} + \frac{\partial^2 F}{\partial y^2} + \frac{\partial^2 F}{\partial z^2}$

Vector calculus identities

$$\nabla \times (\nabla \times \boldsymbol{F}) = \nabla(\nabla \cdot \boldsymbol{F}) - \nabla^2 \boldsymbol{F}$$

Acknowledgements

The work presented in this master thesis was part of a collaboration with Los Alamos National Laboratory (Los Alamos, New Mexico, US). The Laboratory funded the present research and provided the computational resources that were essential in carrying out the simulations.

Dr. Gian Luca Delzanno from T-5 division of LANL supervised the work in collaboration with Dr. Vadim Roytershteyn from Space Science Institute (Boulder, Colorado, US).

References

[1] Richard Mansergh Thorne. «Radiation belt dynamics: The importance of wave-particle interactions». In: *Geophysical Research Letters* 37.22 (2010).

[2] W. J. Burtis and R. A. Helliwell. «Banded chorus - A new type of VLF radiation observed in the magnetosphere by OGO 1 and OGO 3». In: *Journal of Geophysical Research (1896-1977)* 74.11 (1969), pp. 3002–3010.

[3] Bruce T. Tsurutani and Edward J. Smith. «Postmidnight chorus: A substorm phenomenon». In: *Journal of Geophysical Research (1896-1977)* 79.1 (1974), pp. 118–127.

[4] O. Santolik et al. «Oblique propagation of whistler mode waves in the chorus source region». In: *Journal of Geophysical Research: Space Physics* 114.A12 (2009).

[5] Wen Li et al. «Characteristics of the Poynting flux and wave normal vectors of whistler-mode waves observed on THEMIS». In: *Journal of Geophysical Research: Space Physics* 118.4 (2013), pp. 1461–1471.

[6] M. Hayosh, O. Santolik, and M. Parrot. «Location and size of the global source region of whistler mode chorus». In: *Journal of Geophysical Research: Space Physics* 115.A3 (2010).

[7] Danny Summers, Richard M. Thorne, and Fuliang Xiao. «Relativistic theory of wave-particle resonant diffusion with application to electron acceleration in the magnetosphere». In: *Journal of Geophysical Research: Space Physics* 103.A9 (1998), pp. 20487–20500.

[8] Nigel P. Meredith et al. «Outer zone relativistic electron acceleration associated with substorm-enhanced whistler mode chorus». In: *Journal of Geophysical Research: Space Physics* 107.A7 (2002), SMP 29-1-SMP 29–14.

[9] Nigel P. Meredith et al. «Favored regions for chorus-driven electron acceleration to relativistic energies in the Earth's outer radiation belt». In: *Geophysical Research Letters* 30.16 (2003).

[10] Binbin Ni et al. «Chorus wave scattering responsible for the Earth's dayside diffuse auroral precipitation: A detailed case study». In: *Journal of Geophysical Research: Space Physics* 119.2 (2014), pp. 897–908.

[11] Y. Nishimura et al. «Identifying the Driver of Pulsating Aurora». In: *Science* 330.6000 (2010), pp. 81–84.

[12] S. Kasahara et al. «Pulsating aurora from electron scattering by chorus waves». In: *Nature* 554 (Feb. 2018).

[13] M. N. Oliven and D. A. Gurnett. «Microburst phenomena: 3. An association between microbursts and VLF chorus». In: *Journal of Geophysical Research (1896-1977)* 73.7 (1968), pp. 2355–2362.

[14] A. W. Breneman et al. «Observations Directly Linking Relativistic Electron Microbursts to Whistler Mode Chorus: Van Allen Probes and FIREBIRD II». In: *Geophysical Research Letters* 44.22 (2017), pp. 11, 265–11, 272.

[15] N. Dunckel and R. A. Helliwell. «Whistler-mode emissions on the OGO 1 satellite». In: *Journal of Geophysical Research (1896-1977)* 74.26 (1969), pp. 6371–6385.

[16] Christopher T. Russell, Robert E. Holzer, and Edward J. Smith. «OGO 3 observations of ELF noise in the magnetosphere: 1. Spatial extent and frequency of occurrence». In: *Journal of Geophysical Research (1896-1977)* 74.3 (1969), pp. 755–777.

[17] Richard M. Thorne et al. «Plasmaspheric hiss». In: *Journal of Geophysical Research (1896-1977)* 78.10 (1973), pp. 1581–1596.

[18] D. P. Hartley et al. «Statistical Properties of Plasmaspheric Hiss From Van Allen Probes Observations». In: *Journal of Geophysical Research: Space Physics* 123.4 (2018), pp. 2605–2619.

[19] King-Wang Chan and Robert E. Holzer. «ELF hiss associated with plasma density enhancements in the outer magnetosphere». In: *Journal of Geophysical Research (1896-1977)* 81.13 (1976), pp. 2267–2274.

[20] Lawrence R. Lyons, Richard Mansergh Thorne, and Charles F. Kennel. «Pitch-angle diffusion of radiation belt electrons within the plasmasphere». In: *Journal of Geophysical Research (1896-1977)* 77.19 (1972), pp. 3455–3474.

[21] S. Peter Gary. *Theory of Space Plasma Microinstabilities.* first. Cambridge University Press, 1993.

[22] C. F. Kennel and H. E. Petschek. «Limit on stably trapped particle fluxes». In: *J. Geophys. Res.* 71.1 (Jan. 1966), pp. 1–28.

[23] Xin An et al. «On the parameter dependence of the whistler anisotropy instability». In: *J. Geophys. Res. Space Physics* 122 (2017), pp. 2001–2009.

[24] X. Tao et al. «Quasilinear analysis of saturation properties of broadband whistler mode waves». In: *Geophys. Res. Lett.* 44 (2017), pp. 8122–8129.

[25] Francis F. Chen. *Introduction to Plasma Physics and Controlled Fusion.* third. Springer International Publishing, 2016.

[26] Richard Fitzpatrick. *Plasma Physics: An Introduction.* first. CRC Press, 2014.

[27] Paul M. Bellan. *Fundamentals of Plasma Physics.* Cambridge University Press, 2008.

[28] R. L. Stenzel. «Whistler waves in space and laboratory plasmas». In: *J. Geophys. Res.* 104.A7 (1999), pp. 14379–14395.

[29] Xin Tao et al. «Theoretical and numerical studies of chorus waves: A review». In: *Science China Earth Sciences* 62 (2019).

[30] S. Peter Gary et al. «Whistler anisotropy instability with a cold electron component: Linear theory». In: *J. Geophys. Res.* 117.A7 (July 2012).

[31] S. Peter Gary, Kaijun Liu, and Dan Winske. «Whistler anisotropy instability at low electron β: Particle-in-cell simulations». In: *Physics of Plasmas* 18.8 (2011).

[32] K. J. Bowers et al. «0.374 Pflop/s Trillion-Particle Kinetic Modeling of Laser Plasma Interaction on Road-runner». In: *Proc. 2008 ACM/IEEE Conf. Supercomputing (Gordon Bell Prize Finalist Paper)* 63 (Nov. 2008), pp. 1–11.

[33] K.J. Bowers et al. «Ultrahigh performance three-dimensional electromagnetic relativistic kinetic plasma simulation». In: *Phys. Plasmas* 15.055703 (2008).

[34] K.J. Bowers et al. «Advances in petascale kinetic simulations with VPIC and Roadrunner». In: *Journal of Physics: Conference Series* 180.012055 (2009).

[35] Thomas H. Stix. *Waves in Plasmas.* first. AIP-Press, 1992.

[36] John M. Dawson. «Particle simulation of plasmas». In: *Rev. Mod. Phys.* 55 (2 Apr. 1983), pp. 403–447.

[37] N. T. Gladd. «The whistler instability at relativistic energies». In: *The Physics of Fluids* 26.4 (1983), pp. 974–982.

[38] Xiangrong Fu et al. «Whistler anisotropy instabilities as the source of banded chorus: Van Allen Probes observations and particle-in-cell simulations». In: *J. Geophys. Res. Space Physics* 119 (2014), pp. 8288–8298.